A Three-Phase Dual-Active-Bridge DC–DC Converter With Reconfigurable Resonant Network for Efficient Wide Voltage Range Operation

Akif Zia Khan, *Student Member, IEEE*, and K. H. Loo, *Member, IEEE*

***Abstract*—All power converters, including dual-active-bridge (DAB) dc–dc converter, cannot sustain a consistently high-efficiency performance over a wide range of operating conditions, and reconfiguration of operation mode represents a viable solution to this fundamental problem. To meet this challenge, a resonant-type three-phase DAB (3p-DAB) converter incorporating a three-phase reconfigurable resonant network has been proposed in this article. The proposed converter can operate either as a 3p-DAB resonant immittance converter (3p-DABRIC) or a 3p-DAB series resonant converter (3p-DABSRC) to enhance its efficiency performance over a wide range of voltage conversion ratio and output power levels. In addition, the proposed converter offers the flexibility to operate with unity power factor, full-range zero-voltage switching, and enhanced light-load efficiency under varying operating conditions by appropriate selection of the converter's operation mode. Based on a careful loss analysis and verification of the loss model by experimental measurements, it has been found that under wide range variations in voltage conversion ratio and output power levels, 3p-DABSRC delivers a more superior efficiency performance at low to medium power levels, whereas 3p-DABRIC generally achieves a higher efficiency at high power levels, and thus combination of both operation modes leads to an overall wide range high-efficiency performance.**

***Index Terms*—DC–DC power conversion, immittance converters (ICs), resonant power conversion, series resonant network, unity power factor (UPF), zero-voltage switching (ZVS).**

I. Introduction

BIDIRECTIONAL dc–dc converters (BDCs) have been widely investigated over the past several decades because of their wide range adoption in different energy conversion applications, such as electric vehicles [1], [2], solid-state transformers [3], [4], energy storage systems [5], [6], microgrids [7], [8], and vehicle-to-grid operation [9], [10] as illustrated in Fig. 1. For high-power applications where the terminal voltages of BDCs are prone to wide range variations, such as in the interactions of BDCs with various energy storage systems [5], [6], maintaining high power conversion efficiencies over the entire operation range have always been a challenging task to achieve. To accomplish this objective, various topological variants of BDCs have been proposed and investigated in the past.

Among all the investigated BDC-variant topologies, three-phase dual-active-bridge (3p-DAB) converter has been a popular choice for high-power applications because of its superiority over other topologies in terms of greater power-transfer capability with lower root-mean-square (rms) transformer current, smaller size of filter capacitors, lower current ripple, lower component stress, capability of buck/boost operation, higher power density, and modularity [11].

From the topology perspective, the conventional 3p-DAB converter comprises three half bridges at both the primary and secondary sides which are coupled using a three-phase transformer. The conventional 3p-DAB utilizes transformer leakage inductances as the principal energy transfer element and its selection is an important design parameter. From the control perspective, the most prevalent modulation scheme to control 3p-DAB is the single phase-shift (SPS) modulation scheme where the magnitude and sign of the phase-shift between the primary and secondary bridge voltages control the magnitude and direction of the transferred power, respectively. However, employing simple SPS modulation scheme to control 3p-DAB converter results in high rms line currents, particularly under large phase-shift, that leads to high conduction loss. Moreover, deviation of voltage conversion ratio from unity leads to a substantial increase in circulating current within the converter and limits its soft switching range, thus deteriorating its light-load efficiency and making it unsuitable for wide voltage range applications. Although many advanced modulation schemes, such as extended phase-shift, triangular, and trapezoidal modulation schemes [12]–[14] have been proposed for 3p-DAB converter, none of them, however, have managed to completely eliminate reactive power loss, achieve full-range soft switching, and enhanced light-load efficiency under wide voltage range operation.

Manuscript received November 11, 2018; revised February 14, 2019 and April 15, 2019; accepted May 27, 2019. Date of publication June 3, 2019; date of current version November 12, 2019. This work was supported by The Hong Kong Polytechnic University under Central Research Grant G-YBXL. This paper was presented in part at the 10th IEEE International Symposium on Power Electronics for Distributed Generation Systems (PEDG), Xi'an, China, June 2019. Recommended for publication by Associate Editor B. P. McGrath. *(Corresponding author: Akif Zia Khan.)*

The authors are with the Department of Electronic and Information Engineering, The Hong Kong Polytechnic University, Hong Kong, SAR (e-mail: akifzia.khan@connect.polyu.hk; kh.loo@polyu.edu.hk).

Color versions of one or more of the figures in this paper are available online at http://ieeexplore.ieee.org.

Digital Object Identifier 10.1109/TPEL.2019.2920115

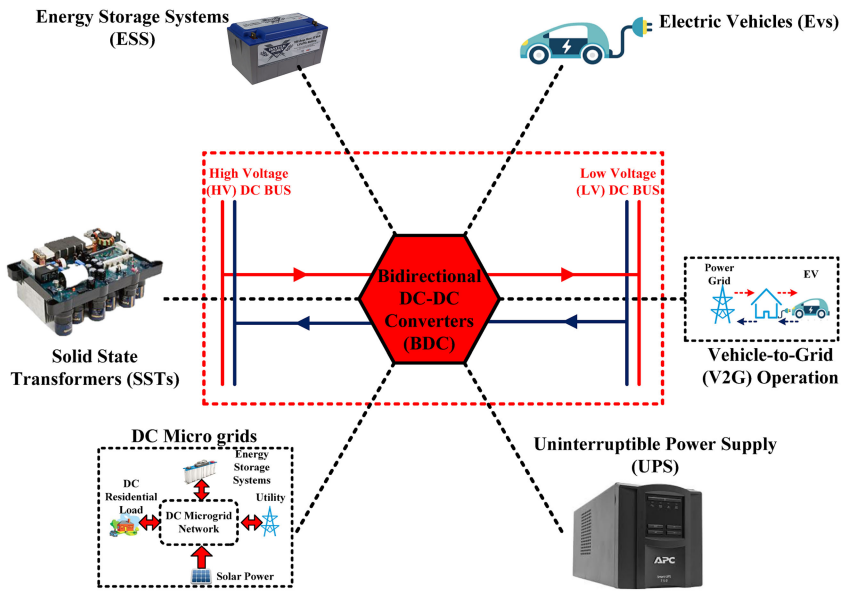

Fig. 1. Application of BDCs in different energy conversion systems.

In conjunction with these advanced modulation techniques, several resonant-type DAB topologies utilizing LC, LCL, CLC, LLC, $CLLC$, and $CLLLC$ resonant networks [15]–[19] have also been investigated extensively in the past but they are also unable to address the aforementioned problems satisfactorily. Three-phase resonant immittance network (3p-RIN) and three-phase series resonant network (3p-SRN) are two such symmetrical resonant networks that offer distinctive advantages under different operating conditions, and when used interchangeably under varying output voltage and power levels, can help to eliminate reactive power loss, achieve full-range soft switching, and enhanced light-load efficiency under wide voltage range operation. A 3p-DAB resonant immittance converter (3p-DABRIC) offers significantly lower rms line currents due to unity power factor (UPF) operation (i.e., eliminating reactive power loss) and the possibility of full-range soft switching irrespective of variation in terminal voltage [20]. However, since 3p-DABRIC utilizes duty cycle modulation to modulate output power, it suffers from increased circulating current at lower output power levels (i.e., when the duty cycles of phase voltages are small), thus deteriorating power conversion efficiency under light-load condition. On the contrary, a 3p-DAB series resonant converter (3p-DABSRC) performs well at low output power when phase-shift is small. However, as phase-shift increases and under wide range variation in terminal voltage, it suffers from high circulating current and hard switching. Therefore, unifying these two resonant networks together into a single *reconfigurable resonant network* and selecting its configuration in accordance with operating conditions (i.e., 3p-DABSRC for low to medium power and 3p-DABRIC for high power) is anticipated to achieve low rms line currents over wide output power range, and hence reduced conduction loss and higher wide range efficiency.

II. Design and Analysis of 3p-RRN

The proposed 3p-RRN has been derived from the networks presented in [20], [21]. The proposed 3p-RRN, as shown in Fig. 2(a), comprises of branch admittances $\mathbf{Y_A}$, $\mathbf{Y_B}$ and switches $S_{\rm N1}$, $S_{\rm N2}$, and $S_{\rm N3}$. The values of passive elements L_1, L_2, C_1, and C_2 are selected such that the branch admittance $\mathbf{Y_A}$ comprising ofpassive elements L_1, C_1 always operates below resonant frequency $\omega_{\rm A}$ and the branch admittance $\mathbf{Y_B}$ comprising passive elements L_2, C_2 always operates above resonant frequency $\omega_{\rm B}$. This implies that the branch admittance $\mathbf{Y_A}$ is capacitive and the branch admittance $\mathbf{Y_B}$ is inductive. Regarding the labeling of the network terminals shown in Fig. 2, the following conventions are adopted—terminals 1, 2, and 3 represent the input ports of the network, whereas terminals 4, 5, and 6 represent the output ports of the network. Furthermore, subscripts $1x$ (where x = A, B, and C) are used to denote the parameters (i.e., line currents and phase voltages) at the input ports of the network, whereas the subscripts $2x$ (where x = A, B, and C) are used to denote the parameters (i.e., line currents and phase voltages) at the output ports of the network.

When switches $S_{\rm N1}$, $S_{\rm N2}$, and $S_{\rm N3}$ are turned ON, the network transforms to a 3p-RIN as shown in Fig. 2(b), and when they are turned OFF, the branch admittance $\mathbf{Y_A}$ is isolated from the network leaving behind the branch admittance $\mathbf{Y_B}$ only. Subsequently, phase transposition is applied at the output ports of the network (i.e., output phase voltages $\mathbf{V_{2A}}$, $\mathbf{V_{2B}}$, and $\mathbf{V_{2C}}$ are phase shifted by 120°) such that the corresponding phase voltages are interfaced via an LC network as shown in Fig. 2(c), transforming a 3p-RIN to a 3p-SRN. It should be noted that for 3p-RIN [cf. Fig. 2(b)], terminal 4 of the network is connected to output phase A, terminal 5 to output phase B, and terminal 6 to output phase C. However for 3p-SRN, since phase transposition is applied at the output ports of the network, output phase A at terminal 4 is effectively transposed to output phase C, output phase B at terminal 5 to output phase A, and output phase C at terminal 6 to output phase B [cf. Fig. 2(c)]. Detailed mathematical analysis for each of the two resonant networks is presented in the following subsections.

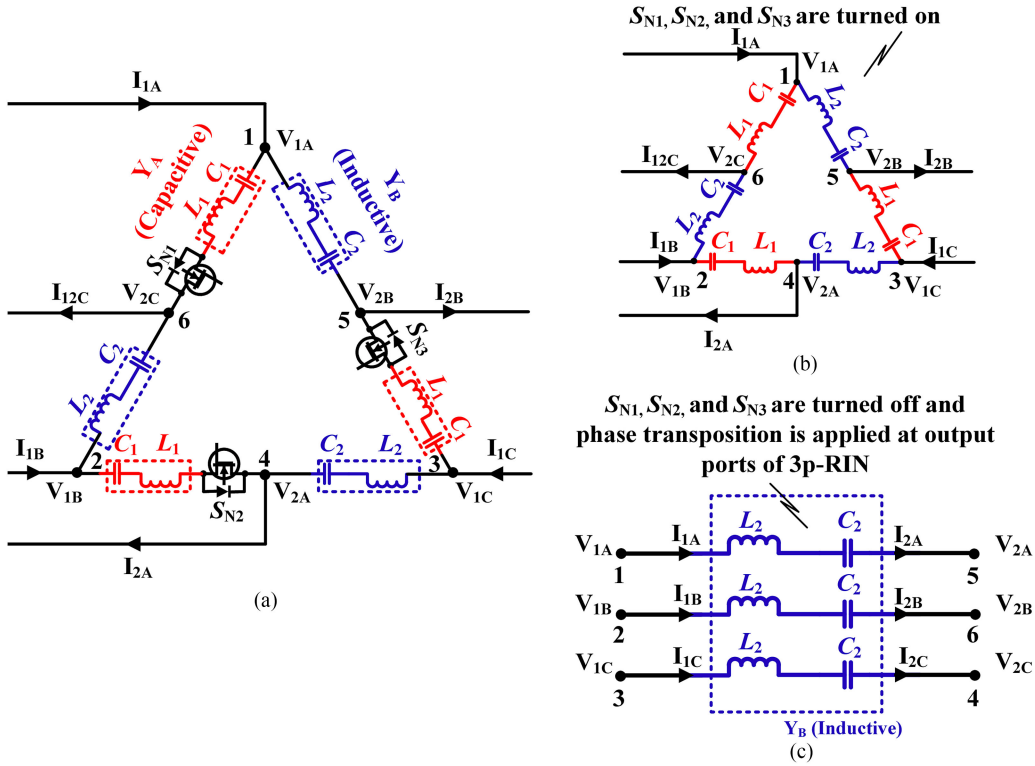

Fig. 2. (a) Proposed 3p-RRN; (b) 3p-RIN; (c) 3p-SRN.

A. *Mathematical Analysis of 3p-RIN Configuration*

For the 3p-RIN shown in Fig. 2(b) to operate as an immittance network, the branch admittances $\mathbf{Y_A}$ and $\mathbf{Y_B}$ have to be equal in magnitude and opposite in phase, i.e., $\mathbf{Y_A} = Y\angle 90^\circ$ and $\mathbf{Y_B} = Y\angle -90^\circ$, thus allowing the branch admittances $\mathbf{Y_A}$ and $\mathbf{Y_B}$ to cancel each other and resonate at the switching frequency. This network is excited by the three-phase input and output voltages in an interlacing manner such that upon satisfaction of the immittance condition, each input line current is a function of two output phase voltages and each output line current is a function of two input phase voltages as given by (1). The derivation of these expressions can be found in [20].

$$\begin{aligned}
\mathbf{I_{1A(3p-RIN)}} &= \mathbf{Y_A}(\mathbf{V_{2C}} - \mathbf{V_{2B}}) \\
\mathbf{I_{1B(3p-RIN)}} &= \mathbf{Y_A}(\mathbf{V_{2A}} - \mathbf{V_{2C}}) \\
\mathbf{I_{1C(3p-RIN)}} &= \mathbf{Y_A}(\mathbf{V_{2B}} - \mathbf{V_{2A}}) \\
\mathbf{I_{2A(3p-RIN)}} &= \mathbf{Y_A}(\mathbf{V_{1C}} - \mathbf{V_{1B}}) \\
\mathbf{I_{2B(3p-RIN)}} &= \mathbf{Y_A}(\mathbf{V_{1A}} - \mathbf{V_{1C}}) \\
\mathbf{I_{2C(3p-RIN)}} &= \mathbf{Y_A}(\mathbf{V_{1B}} - \mathbf{V_{1A}}). \qquad (1)
\end{aligned}$$

Considering that the network and the phase voltages are balanced, i.e., $|\mathbf{V_{1A}}| = |\mathbf{V_{1B}}| = |\mathbf{V_{1C}}| = V_1$ and $|\mathbf{V_{2A}}| = |\mathbf{V_{2B}}| = |\mathbf{V_{2C}}| = V_2$, the phase voltages at the input and output ports of the 3p-RIN can be written in phasor form as $\mathbf{V_{1A}} = V_1\angle 0^\circ$, $\mathbf{V_{1B}} = V_1\angle 120^\circ$, $\mathbf{V_{1C}} = V_1\angle -120^\circ$, $\mathbf{V_{2A}} = V_2\angle 0^\circ + \beta$, $\mathbf{V_{2B}} = V_2\angle 120^\circ + \beta$, $\mathbf{V_{2C}} = V_2\angle -120^\circ + \beta$ where β is the phase-shift between the input and output voltages of the same phase, e.g. $v_{1A}(t)$ and $v_{2A}(t)$. Assuming $\mathbf{Y_A}$ is overall capacitive, $\mathbf{Y_A}$ can be expressed in phasor form as $\mathbf{Y_A} = Y\angle 90^\circ$ where Y is the magnitude of the branch admittances $\mathbf{Y_A}$ and $\mathbf{Y_B}$ at the switching frequency. By simplification of (1) taking into consideration the above assumptions, the following expressions are obtained that depict the phasor relationship between phase voltages and line currents at the input and output ports of the 3p-RIN:

$$\begin{aligned}
\mathbf{I_{1A(3p-RIN)}} &= (\sqrt{3}\,YV_2)\angle 0^\circ + \beta = \sqrt{3}\,Y\mathbf{V_{2A}} \\
\mathbf{I_{1B(3p-RIN)}} &= (\sqrt{3}\,Y\,V_2)\angle 120^\circ + \beta = \sqrt{3}\,Y\mathbf{V_{2B}} \\
\mathbf{I_{1C(3p-RIN)}} &= (\sqrt{3}\,YV_2)\angle -120^\circ + \beta = \sqrt{3}\,Y\mathbf{V_{2C}} \\
\mathbf{I_{2A(3p-RIN)}} &= (\sqrt{3}\,YV_1)\angle 0^\circ = \sqrt{3}\,Y\mathbf{V_{1A}} \\
\mathbf{I_{2B(3p-RIN)}} &= (\sqrt{3}\,YV_1)\angle 120^\circ = \sqrt{3}\,Y\mathbf{V_{1B}} \\
\mathbf{I_{2C(3p-RIN)}} &= (\sqrt{3}\,YV_1)\angle -120^\circ = \sqrt{3}\,Y\mathbf{V_{1C}} \qquad (2)
\end{aligned}$$

where

$$|\mathbf{I_{1A(3p-RIN)}}| = |\mathbf{I_{1B(3p-RIN)}}| = |\mathbf{I_{1C(3p-RIN)}}| = (\sqrt{3}\,YV_2)$$

and

$$|\mathbf{I_{2A(3p-RIN)}}| = |\mathbf{I_{2B(3p-RIN)}}| = |\mathbf{I_{2C(3p-RIN)}}| = (\sqrt{3}\,YV_1).$$

From the above expressions, it can be observed that the line current at an input port is a function of (and in-phase with) the phase voltage at the corresponding output port of the 3p-RIN, e.g., $i_{1A}(t) = f(v_{2A}(t))$. Similarly, the line current

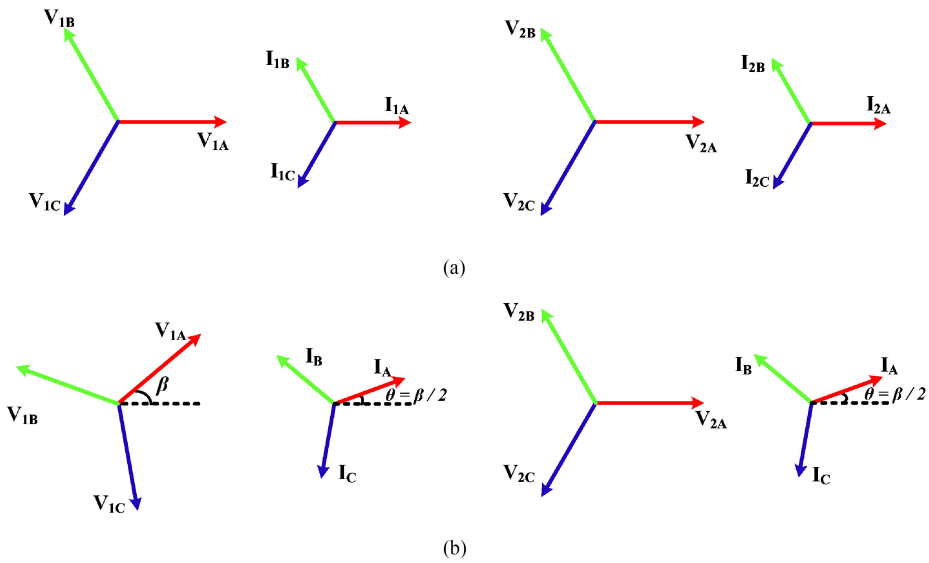

Fig. 3. (a) Phasor diagrams for 3p-RIN with $\beta = 0°$. (b) Phasor diagrams for 3p-SRN with unity voltage conversion ratio.

at an output port is a function of (and in-phase with) the phase voltage at the corresponding input port of the 3p-RIN, e.g., $i_{2\mathrm{A}}(t) = f(v_{1\mathrm{A}}(t))$. In concurrence to this, the phase-shift angle β can be used to achieve the desired power factor at the input and output ports of the 3p-RIN. For $\beta = 0$, all phase voltages at the input and output ports will be in phase with their respective line currents resulting in UPF operation. For $\beta > 0$, the phase voltages at the input and output ports will have a phase displacement of β with their respective line currents resulting in lagging power factor at the input port and leading power factor at the output port.

B. Mathematical Analysis of 3p-SRN Configuration

When switches S_{N1}, S_{N2}, and S_{N3} are turned OFF and phase transposition is applied at the output ports of the 3p-RRN, the resonant network is transformed into a 3p-SRN as shown in Fig. 2(c). The line currents for this resonant network configuration are given by the following expressions:

$$\begin{aligned}\mathbf{I_{1A(3p-SRN)}} &= \mathbf{Y_B}(\mathbf{V_{1A}} - \mathbf{V_{2A}})\\ \mathbf{I_{1B(3p-SRN)}} &= \mathbf{Y_B}(\mathbf{V_{1B}} - \mathbf{V_{2B}})\\ \mathbf{I_{1C(3p-SRN)}} &= \mathbf{Y_B}(\mathbf{V_{1C}} - \mathbf{V_{2C}}).\end{aligned} \tag{3}$$

As the branch admittance $\mathbf{Y_B}$ is overall inductive, i.e.,$\mathbf{Y_B} = Y\angle -90°$, the phasor relationship between line currents and phase voltages of 3p-SRN is given as follows:

$$\begin{aligned}\mathbf{I_{1A(3p-SRN)}} &= I_{1(3\mathrm{p-SRN})}\angle 0° + \theta\\ \mathbf{I_{1B(3p-SRN)}} &= I_{1(3\mathrm{p-SRN})}\angle 120° + \theta\\ \mathbf{I_{1C(3p-SRN)}} &= I_{1(3\mathrm{p-SRN})}\angle -120° + \theta\end{aligned} \tag{4}$$

where $|\mathbf{I_{1A(3p-SRN)}}| = |\mathbf{I_{1B(3p-SRN)}}| = |\mathbf{I_{1C(3p-SRN)}}| = I_{1(3\mathrm{p-SRN})} = \sqrt{Y^2((-V_2\sin(\beta))^2 + (V_2\cos(\beta) - V_1)^2)}$ and $\theta = \tan^{-1}(\frac{V_1 - V_2\cos(\beta)}{V_2\sin(\beta)})$.

By comparing the expressions for the line currents of 3p-RIN and 3p-SRN given by (2) and (4), it is interesting to note that for 3p-RIN, the phase angles of the input and output line currents are insensitive to variations in the input and output phase voltages. This intrinsic attribute of 3p-RIN provides a mechanism to independently control the phase angles of the input and output line currents irrespective of variations in the input and output phase voltages. However, for 3p-SRN, the phase angles of the input and output line currents are functions of the input and output phase voltages and can be determined using (4).

C. Phasor Diagram Representations of Two Network Configurations

The phasor diagrams corresponding to (2) for 3p-RIN are shown in Fig. 3(a), and the phasor diagrams corresponding to (4) for 3p-SRN are depicted in Fig. 3(b). The phasor diagrams for 3p-RIN are considered for the case when $\beta = 0°$. Under this condition, the phase voltages and line currents at the input and output ports are in phase resulting in UPF at both input and output ports of 3p-RIN. This mode of operation is utilized to achieve UPF in 3p-DABRIC and results in significantly reduced rms line currents and zero reactive power loss.

The phasor diagrams for 3p-SRN are considered for the case when the phase-shift angle $\beta > 0°$ and the voltage conversion ratio is unity, i.e., $V_1 = V_2$. For this particular case, the phase angle θ of the line current is given by $\theta = \frac{\beta}{2}$. This causes the line current to lag the input phase voltage and lead the output phase voltage by θ as shown in Fig. 3(b). It also results in full-range ZVS operation of 3p-DABSRC. In the case of non-unity voltage conversion ratio, the ZVS region of 3p-DABSRC will be restricted and can be computed using (4) where the phase angle θ of the line current must lie within the range $0° \leq \theta \leq \beta$ in order to realize ZVS commutation for all switches.

III. Proposed 3p-DAB Reconfigurable Resonant Converter

The proposed 3p-DAB converter as shown in Fig. 4 comprises 3p-full bridge in the primary side and 3p-half bridge in

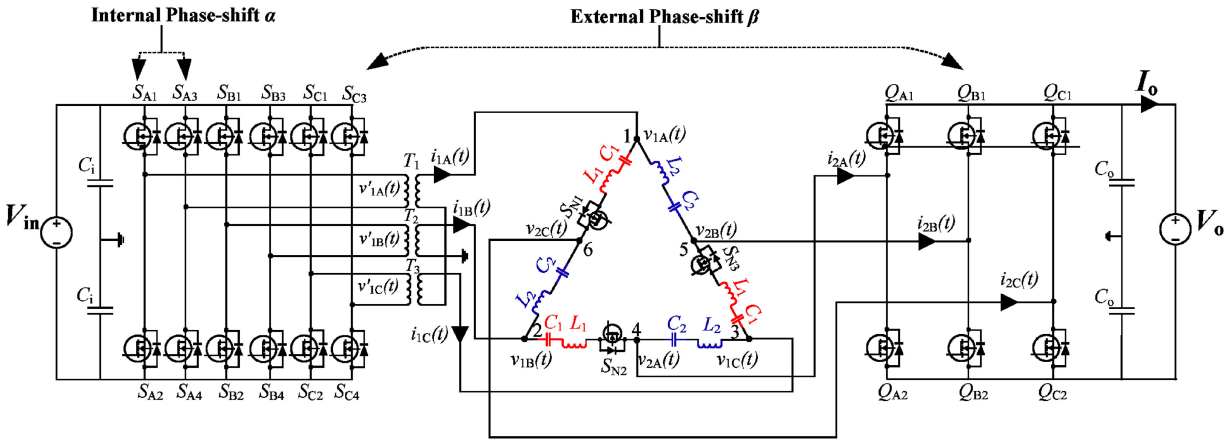

Fig. 4. Proposed 3p-DAB converter with 3p-RRN.

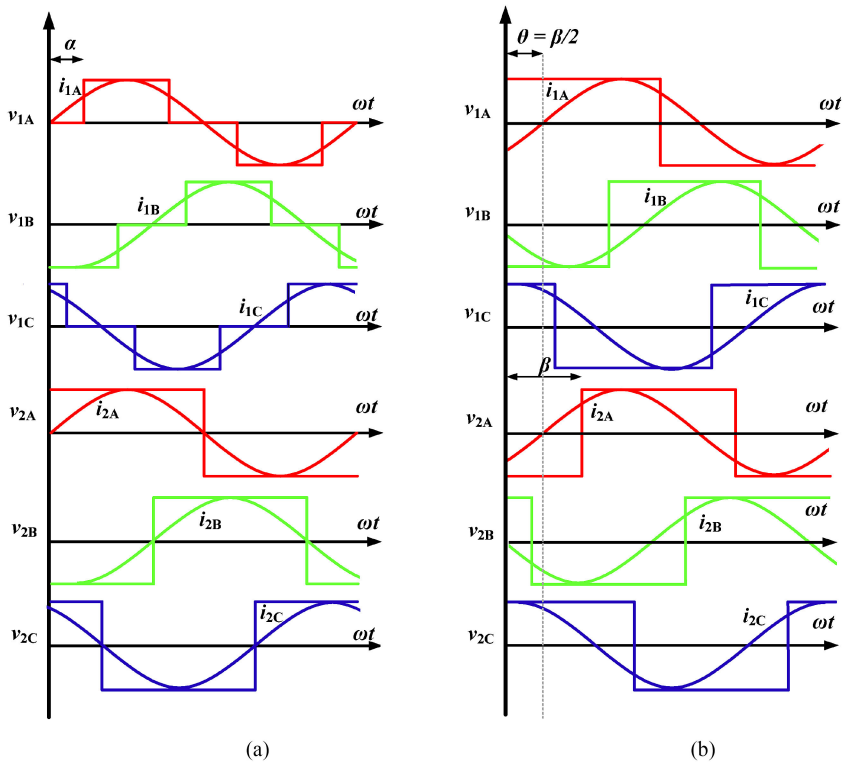

Fig. 5. Operating waveforms of the proposed converter for (a) 3p-DABRIC considering UPF operation i.e. $\beta = 0\,^{\circ}$. (b) 3p-DABSRC controlled with SPS modulation considering unity voltage conversion ratio, i.e., $V_{1A} = V_{2A}$.

the secondary side connected by three single-phase open delta-wye configured transformers and a 3p-RRN. Depending upon the state of switches S_{N1}, S_{N2}, and S_{N3} in the 3p-RRN, the proposed converter can be operated either as a 3p-DABRIC or as a 3p-DABSRC. The proposed converter offer two degrees of freedom, i.e., internal phase-shift angle α and external phase-shift angle β for modulating output power. Duty cycle modulation is used to control 3p-DABRIC [16] where internal phase-shift angle α is utilized to modulate the duty cycle of primary bridge voltages and hence control the output power of 3p-DABRIC, whereas SPS modulation is used to control 3p-DABSRC where external phase-shift angle β between the primary and secondary bridge voltages is used to modulate the output power of 3p-DABSRC [22]. The operating waveforms for both operation modes are shown in Fig. 5. A detailed modeling and analysis of the proposed converter is presented in the following sections.

IV. Modeling and Analysis of the Proposed Converter

A. Assumptions

The following assumptions are made to simplify the mathematical analysis of the proposed 3p-DAB converter while highlighting its key features.

1) The branch admittances $\mathbf{Y_A}$ and $\mathbf{Y_B}$ are identical.

2) The leakage inductances of transformers are assumed to be small and are ignored in the analysis.
3) All passive components and switches are assumed to be ideal.
4) The input dc bus voltage $V_{\rm in}$ is assumed to be constant, while the output dc bus voltage $V_{\rm o}$ is assumed to vary over a wide range.
5) Both 3p-DABRIC and 3p-DABSRC have the same maximum output power.

B. Power Flow Analysis for 3p-DABRIC

When switches $S_{\rm N1}$, $S_{\rm N2}$, and $S_{\rm N3}$ in the 3p-RRN are turned ON, the proposed converter transforms to a 3p-DABRIC. To perform power flow analysis, all the primary-side parameters are reflected to the secondary side of the transformers to simplify the analysis. By means of fundamental component analysis, the input and output phase voltages of the 3p-RIN can be expressed by

$$v_{1\gamma}(t) = \frac{4V_{\rm in}\cos(\alpha)}{n\pi}\sin\left(\omega t + f(\gamma)\frac{2\pi}{3}\right)$$
$$v_{2\gamma}(t) = \frac{2V_{\rm o}}{\pi}\sin\left(\omega t + f(\gamma)\frac{2\pi}{3}\right) \quad (5)$$

where $f(\gamma) = (0,+1,-1)$ when $\gamma = ({\rm A, B, C})$ and $n = \frac{N_p}{N_s}$ is the transformer's turn ratio. It is important to mention that the above expressions represent the input phase voltages of the 3p-RIN with respect to the transformer's star point, whereas the output phase voltages are referred to the output dc bus midpoint. To determine the expressions for the line currents of 3p-DABRIC, (5) can be substituted into the time-domain expressions of (2) to yield the time functions of the line currents. For example, the input and output line currents of 3p-RIN for phase A are given by the following:

$$i_{1{\rm A}(3{\rm p-DABRIC})}(t) = \frac{2\sqrt{3}\ V_{\rm o}Y_{3{\rm p-DABRIC}}}{\pi}\sin(\omega t+\beta)$$
$$i_{2{\rm A}(3{\rm p-DABRIC})}(t) = \frac{4\sqrt{3}\ V_{\rm in}Y_{3{\rm p-DABRIC}}}{n\pi}\cos(\alpha)\sin(\omega t) \quad (6)$$

where $Y_{3{\rm p-DABRIC}}$ is the magnitude of branch admittances $\mathbf{Y_A}$ and $\mathbf{Y_B}$ for 3p-DABRIC operated with switching frequency $f_{{\rm S}(3{\rm p-DABRIC})}$. The average output power $P_{{\rm o}(3{\rm p-DABRIC})}$ can be obtained from (5) and (6) for a single phase and multiplying the resulting expression by three

$$P_{{\rm o}(3{\rm p-DABRIC})} = \frac{3}{2\pi}\int_0^{2\pi} v_{2{\rm A}}(t)i_{2{\rm A}(3{\rm p-DABRIC})}(t)\ dt = \frac{12\sqrt{3}V_{\rm o}V_{\rm in}Y_{3{\rm p-DABRIC}}}{n\pi^2}\cos(\alpha)\cos(\beta). \quad (7)$$

Since only UPF operation is considered for 3p-DABRIC where internal phase-shift angle α is controlled to modulate output power, β is set to 0° to yield the output power expression for 3p-DABRIC as given as follows:

$$P_{{\rm o}(3{\rm p-DABRIC})} = \frac{12\sqrt{3}V_{\rm o}V_{\rm in}Y_{3{\rm p-DABRIC}}}{n\pi^2}\cos(\alpha). \quad (8)$$

The expression for output current $I_{{\rm o}(3{\rm p-DABRIC})}$ can be obtained by dividing (8) with output terminal voltage $V_{\rm o}$ yielding

$$I_{{\rm o}(3{\rm p-DABRIC})} = \frac{12\sqrt{3}V_{\rm in}Y_{3{\rm p-DABRIC}}}{n\pi^2}\cos(\alpha). \quad (9)$$

C. Power Flow Analysis for 3p-DABSRC Configuration

When switches $S_{\rm N1}$, $S_{\rm N2}$, and $S_{\rm N3}$ in the 3p-RRN are turned OFF, the proposed converter transforms to a 3p-DABSRC. This operation isolates the capacitive branches $\mathbf{Y_A}$ from the network and utilizes the inductive branches $\mathbf{Y_B}$ only. Referring to Fig. 6(b), when $S_{\rm N1}$ (the same argument applies to $S_{\rm N2}$ and $S_{\rm N3}$) is turned OFF, the capacitor C_1 of the capacitive branch $\mathbf{Y_A}$ is charged to the maximum voltage $(\frac{V_{\rm in}}{n}+\frac{V_o}{2})$ by the voltage difference $v_{1{\rm A}} - v_{2{\rm C}}$. As a result, the voltage seen by $S_{\rm N1}$, i.e., $v_{1{\rm A}} - v_{2{\rm C}} - v_{\rm cap16}$ will vary between 0 and $-2(\frac{V_{\rm in}}{n}+\frac{V_o}{2})$ which will always keep the body diode of $S_{\rm N1}$ in a reverse-biased state. Therefore, the capacitive branch $\mathbf{Y_A}$ can be fully isolated by using a two-quadrant switch when the converter operates as 3p-DABSRC. Furthermore, to operate the proposed converter as a 3p-DABSRC, phase transposition must be applied at the output ports of the 3p-SRN, i.e., output phase voltages are to be phase-shifted by 120° so that the phase voltages at the input and output ports of the 3p-SRN correspond with each other. To obtain the expressions for the line currents of 3p-DABSRC, (5) can be substituted in the time-domain expressions of (3) to yield the time functions of the line currents. For example, the input and output line currents of 3p-SRN for phase A can be represented as follows as given on the top of next page eq. (10) shown at the bottom of this page.

Similar to 3p-DABRIC, the average output power $P_{{\rm o}(3{\rm p-DABSRC})}$ can be obtained from (5) and (10) for a single phase and multiplying the resulting expression by three

$$P_{{\rm o}(3{\rm p-DABSRC})} = \frac{3}{2\pi}\int_0^{2\pi} v_{1{\rm A}}(t)i_{1{\rm A}(3{\rm p-DABSRC})}(t)\ dt = \frac{12V_{\rm o}V_{\rm in}Y_{(3{\rm p-DABSRC})}}{n\pi^2}\cos(\alpha)\sin(\beta). \quad (11)$$

Since only SPS operation is considered for 3p-DABSRC where external phase-shift angle β is controlled to modulate output power, α is set to 0° in the above equation to yield the output

$$i_{1{\rm A}(3{\rm p-DABSRC})}(t) = i_{2{\rm A}(3{\rm p-DABSRC})}(t) = \frac{(2V_{\rm o}n\cos(\beta)\cos(\omega t) - 4V_{\rm in}\cos(\alpha)\cos(\omega t) + 2V_{\rm o}n\sin(\beta)\sin(\omega t))Y_{3{\rm p-DABSRC}}}{n\pi} \quad (10)$$

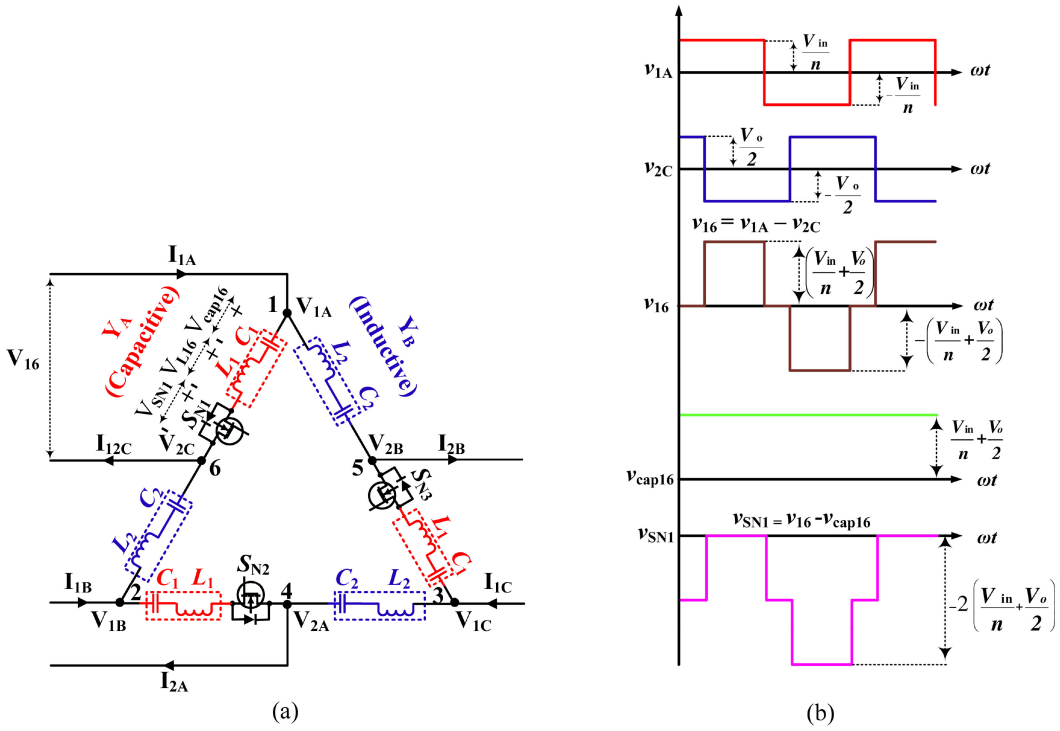

Fig. 6. (a) Voltage across branch $\mathbf{Y_A}$ and switch $S_{\rm N1}$ for 3p-DABSRC configuration. (b) Voltage waveforms across capacitor C_1 and switch $S_{\rm N1}$ for 3p-DABSRC configuration.

power for an SPS-controlled 3p-DABSRC given by

$$P_{\rm o(3p-DABSRC)} = \frac{12V_{\rm o}V_{\rm in}Y_{\rm (3p-DABSRC)}}{n\pi^2}\sin(\beta). \tag{12}$$

The expression for output current $I_{\rm o(3p-DABSRC)}$ can be obtained by dividing (12) with output terminal voltage $V_{\rm o}$ yielding

$$I_{\rm o(3p-DABSRC)} = \frac{12V_{\rm in}Y_{\rm (3p-DABSRC)}}{n\pi^2}\sin(\beta). \tag{13}$$

D. Design Procedure and Selection of Component Values

For 3p-DABRIC, the resonant frequency at which the branch admittances $\mathbf{Y_{A(3p-DABRIC)}}$ and $\mathbf{Y_{B(3p-DABRIC)}}$ resonate with each other can be found by solving $|\mathbf{Y_{A(3p-DABRIC)}}| = |\mathbf{Y_{B(3p-DABRIC)}}|$ which gives

$$\omega_{\rm R} = 2\pi f_{\rm S(3p-DABRIC)} = \sqrt{\frac{(C_1+C_2)}{C_1C_2(L_1+L_2)}}. \tag{14}$$

Subsequently, at resonant frequency $\omega_{\rm R}$, the magnitude $Y_{\rm 3p-DABRIC}$ of the branch admittances $\mathbf{Y_{A(3p-DABRIC)}}$ and $\mathbf{Y_{B(3p-DABRIC)}}$ can be found by calculating the equivalent admittance of L_1, C_1 constituting $\mathbf{Y_{A(3p-DABRIC)}}$ and L_2, C_2 constituting $\mathbf{Y_{B(3p-DABRIC)}}$ which gives

$$|\mathbf{Y_{A(3p-DABRIC)}}| = Y_{\rm (3p-DABRIC)} = \left|\frac{\omega_{\rm R}C_1}{\omega_{\rm R}L_1\left(\omega_{\rm R}C_1 - \frac{1}{\omega_{\rm R}L_1}\right)}\right| \text{(capacitive)}$$

$$|\mathbf{Y_{B(3p-DABRIC)}}| = Y_{\rm (3p-DABRIC)} = \left|\frac{\omega_{\rm R}C_2}{\omega_{\rm R}L_2\left(\omega_{\rm R}C_2 - \frac{1}{\omega_{\rm R}L_2}\right)}\right| \text{(inductive)}. \tag{15}$$

Note that the angular series-resonant frequencies $\omega_{\rm A}$ and $\omega_{\rm B}$ of branch admittances $\mathbf{Y_{A(3p-DABRIC)}}$ and $\mathbf{Y_{B(3p-DABRIC)}}$ are given by

$$\omega_{\rm A} = \frac{1}{\sqrt{L_1C_1}}\ \omega_{\rm B} = \frac{1}{\sqrt{L_2C_2}}. \tag{16}$$

The relationship between the resonant frequencies $\omega_{\rm A}$, $\omega_{\rm B}$, $\omega_{\rm R}$, and the magnitude $Y_{\rm 3p-DABRIC}$ of branch admittances $\mathbf{Y_{A(3p-DABRIC)}}$ and $\mathbf{Y_{B(3p-DABRIC)}}$ can be determined by substituting the expressions for L_1 and L_2 from (16) into (15) and the results are given by

$$|\mathbf{Y_{A(3p-DABRIC)}}| = Y_{\rm (3p-DABRIC)} = \frac{\omega_{\rm R}C_1}{1-\left(\frac{\omega_{\rm R}}{\omega_{\rm A}}\right)^2} \ni \omega_{\rm A} > \omega_{\rm R} \text{ (capacitive)}$$

$$|\mathbf{Y_{B(3p-DABRIC)}}| = Y_{\rm (3p-DABRIC)} = \frac{\omega_{\rm R}C_2}{\left(\frac{\omega_{\rm R}}{\omega_{\rm B}}\right)^2-1} \ni \omega_{\rm B} < \omega_{\rm R} \text{ (inductive)}. \tag{17}$$

The ratios $\frac{\omega_{\rm R}}{\omega_{\rm A}}$ and $\frac{\omega_{\rm R}}{\omega_{\rm B}}$ in the denominator of (17) determine the voltage stresses across the passive components, line current waveforms, and the size of passive components in the 3p-RIN.

To achieve near-sinusoidal line current waveforms and minimum component stresses, the angular series resonant frequencies are selected as follows:

$$\omega_{\rm A} = 1.2\omega_{\rm R}, \quad \omega_{\rm B} = 0.8\omega_{\rm R}. \tag{18}$$

For a given power rating, terminal voltages, and switching frequency, the values of passive components L_1, L_2, C_1, and C_2 can be obtained by using expressions (15)–(18).

E. Switching Frequencies for Both Configurations

Once the values of the passive components L_1, L_2, C_1, and C_2 have been determined, it can be observed upon comparing (8) and (12) that a 3p-DABRIC can transfer a maximum power which is $\sqrt{3}$ times higher than that of a 3p-DABSRC with the same passive component values L_1, L_2, C_1, and C_2. Furthermore, by comparing (8) and (12), it can also be found that in order to achieve the same maximum output power for both configurations, the magnitude of the branch admittances of 3p-DABRIC should be $\sqrt{3}$ times smaller than those of 3p-DABSRC, or mathematically

$$Y_{(3{\rm p-DABSRC})} = \sqrt{3} Y_{(3{\rm p-DABRIC})}. \tag{19}$$

Hence, for a given value of switching frequency $f_{{\rm s}(3{\rm p-DABRIC})}$ for 3p-DABRIC, the corresponding switching frequency $f_{{\rm s}(3{\rm p-DABSRC})}$ for 3p-DABSRC can be found from (20) shown at the bottom of this page.

Substituting the expression for L_2C_2 from (16) into (20) yields the switching frequency $f_{{\rm s}(3{\rm p-DABSRC})}$ for 3p-DABSRC in terms of the resonant frequency $\omega_{\rm R}$ and the series resonant frequency $\omega_{\rm B}$ of the branch admittance $\mathbf{Y}_{\rm B}$ as

$$f_{{\rm s}(3{\rm p-DABSRC})} = \lambda f_{{\rm s}(3{\rm p-DABRIC})}$$
$$\text{where } \lambda = \frac{\sqrt{3}\left(\sqrt{\left(\frac{\omega_{\rm R}}{\omega_{\rm B}}\right)^4 + 10\left(\frac{\omega_{\rm R}}{\omega_{\rm B}}\right)^2 + 1} + \left(\frac{\omega_{\rm R}}{\omega_{\rm B}}\right)^2 - 1\right)}{6\left(\frac{\omega_{\rm R}}{\omega_{\rm B}}\right)^2}. \tag{21}$$

By substituting the value of $\left(\frac{\omega_{\rm R}}{\omega_{\rm B}}\right)$ specified in (18) into (21), λ is found to have a value of 0.91, i.e.,

$$f_{{\rm s}(3{\rm p-DABSRC})} = 0.91 f_{{\rm s}(3{\rm p-DABRIC})}. \tag{22}$$

The relationship given by (22) holds true for any specification of the proposed converter as long as the values of the passive elements L_2 and C_2 are selected in compliance with (18).

V. Prototype Design and the Experimental Results

To validate the effectiveness and benchmark the performance of the proposed converter, a laboratory prototype was designed and built following the design procedure mentioned in Section IV. The specifications and components used for the laboratory prototype are listed in Table I. The prototype was extensively tested for both configurations under wide range variations in voltage conversion ratio and output power. In the following discussions, the voltage conversion ratio of the proposed converter is defined as

$$G = \frac{V_{2\rm A}}{V_{1\rm A}} = \frac{nV_{\rm o}}{2V_{\rm in}}. \tag{23}$$

According to (23), voltage conversion ratio G varies when the terminal voltages $V_{\rm in}$ and/or $V_{\rm o}$ of the converter varies. Since it has been assumed that $V_{\rm in}$ is well regulated, the following discussion considers variation in G due to variation in $V_{\rm o}$ only. Therefore, the terms $V_{\rm o}$ and G are used interchangeably in the following discussions. $V_{\rm o}$ is considered to be varying in the range 0− 225 V and has a nominal value of 150 V. Over this output voltage range, G will vary in the range 0− 1.5. Furthermore, by normalizing output power by the rated output power, the maximum normalized output power corresponding to $G = 1.5$ is 1.5. Hence, for a given voltage conversion ratio G, the normalized output power $P_{\rm o,p.u.}$ can vary in the range of 0–G.

The subsequent discussion compares the performance of both configurations in terms of rms line currents, soft switching operation, and power conversion efficiencies obtained from both loss model and experimental measurements.

A. Comparison of Input Line Currents $I_{1{\rm A,rms}}$

The expressions for the rms input line currents $I_{1{\rm A,rms}}$ for both configurations are given below

$$I_{1{\rm A,rms}(3{\rm p-DABRIC})} = \sqrt{\frac{1}{2\pi}\int_0^{2\pi} [i_{1{\rm A}(3{\rm p-DABRIC})}(t)]^2 d\omega t}$$
$$= \frac{\sqrt{6}\, V_{\rm o} Y_{3{\rm p-DABRIC}}}{\pi} \tag{24}$$

$$I_{1{\rm A,rms}(3{\rm p-DABSRC})} = \sqrt{\frac{1}{2\pi}\int_0^{2\pi} [i_{1{\rm A}(3{\rm p-DABSRC})}(t)]^2 d\omega t}$$
$$= \frac{(\sqrt{2V_{\rm o}^2 n^2 - 8V_{\rm in}V_{\rm o} n\cos(\beta) + 8V_{\rm in}^2}) Y_{3{\rm p-DABSRC}}}{n\pi}. \tag{25}$$

Fig. 7(a)–(c) plots the input line currents $I_{1{\rm A,rms}(3{\rm p-DABRIC})}$ and $I_{1{\rm A,rms}(3{\rm p-DABSRC})}$ versus normalized output power $P_{\rm o,p.u}$ for $G = 0.5$, 1.0, and 1.5 respectively. The curves in Fig. 7(a)–(c) are plotted by using expressions (8), (12), (24), and (25). To keep all figures consistent, red solid lines are used to plot the curves for 3p-DABRIC, whereas blue-dashed lines are used to plot the curves for 3p-DABSRC. As illustrated by Fig. 7(a)–(c), for a particular value of $V_{\rm o}$, $I_{1{\rm A,rms}(3{\rm p-DABRIC})}$ remains constant for the entire output power range and increases with increasing $V_{\rm o}$, while $I_{1{\rm A,rms}(3{\rm p-DABSRC})}$ varies

$$f_{{\rm S}(3{\rm p-DABSRC})} = \frac{\sqrt{3}(\sqrt{16\pi^4 C_2^2 L_2^2 f_{{\rm s}(3{\rm p-DABRIC})}^4 + 40\pi^2 C_2 L_2 f_{{\rm s}(3{\rm p-DABRIC})}^2 + 1} + 4\pi^2 C_2 L_2 f_{{\rm s}(3{\rm p-DABRIC})}^2 - 1)}{24\pi^2 C_2 L_2 f_{{\rm s}(3{\rm p-DABRIC})}} \tag{20}$$

TABLE I
LABORATORY PROTOTYPE SPECIFICATIONS

Input Voltage V_{in}	300 V
Nominal Output Voltage V_{o}	150 V
Output Voltage Range	0-225 V
Rated Output Power P_{o}	1.5 kW
Proposed 3p-RRN component values (L_1, L_2, C_1, C_2)	(285.3 μH, 332.6 μH, 153.4 nF, 306.3 nF)
Switching Frequency for 3p-DABRIC Configuration $f_{\text{S(3p-DABRIC)}}$	20 kHz
Switching Frequency for 3p-DABSRC Configuration $f_{\text{S(3p-DABSRC)}}$	18.2 kHz
Transformer's Turn Ratio n	4
MOSFETs	UJC06505K (650 V, 36.5 A, 45 mΩ)
Transformers core shape and material	3 X N87 Ferrite (E-70 Core)
Inductors core shape and material	6 X N87 Ferrite (E-70 Core)
Controller	Texas Instruments TMS320F28337D

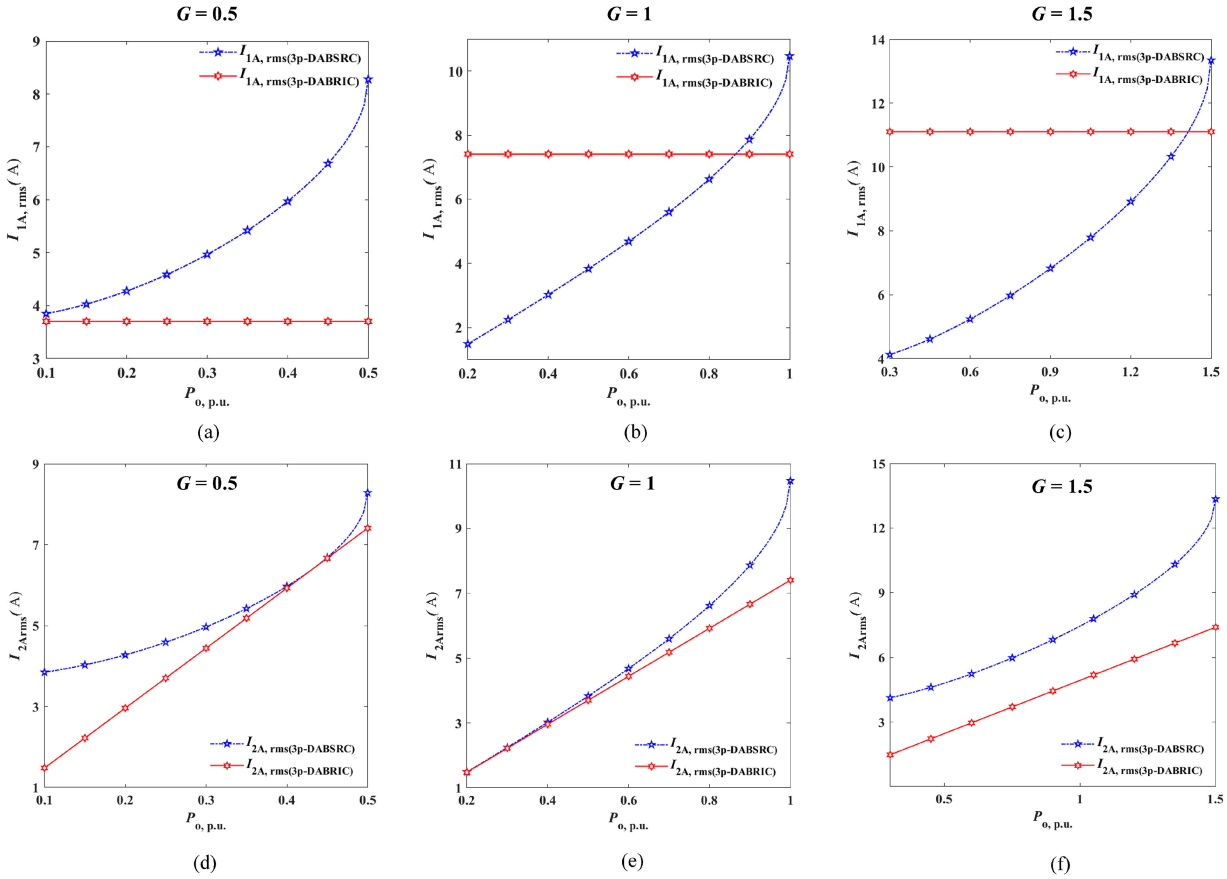

Fig. 7. Comparison of input line current $I_{1\text{A,rms}}$ between 3p-DABRIC and 3p-DABSRC for (a) $G = 0.5$; (b) $G = 1$; (c) $G = 1.5$. Comparison of output line current $I_{2,\text{rms}}$ between 3p-DABRIC and 3p-DABSRC for (d) $G = 0.5$; (e) $G = 1$; (f) $G = 1.5$.

with both G and $P_{\text{o,p.u}}$. It can be observed that for $G = 0.5$ [cf. Fig. 7(a)], $I_{1\text{A,rms(3p-DABRIC)}}$ is always smaller than $I_{1\text{A,rms(3p-DABSRC)}}$. However, for the two other cases when $G > 0.5$ [cf. Fig. 7(b)–(c)], $I_{1\text{A,rms(3p-DABRIC)}}$ is significantly greater than $I_{1\text{A,rms(3p-DABSRC)}}$ at low power levels implying that 3p-DABRIC suffers from higher circulating current in the primary bridge due to duty cycle modulation of the input phase voltages, i.e., due to circulating current flow during the zero voltage level of the input phase voltage. The two curves intersect with each other at high power levels where $I_{1\text{A,rms(3p-DABRIC)}}$

becomes smaller than $I_{1\mathrm{A,rms(3p-DABSRC)}}$. The intersection between the two curves at high power levels occurs as a result of the increase in the external phase-shift angle β of 3p-DABSRC which leads to increased reactive power loss. It can, therefore, be concluded from Fig. 7(a)–(c) that 3p-DABRIC suffers from the drawback of high circulating current at low to medium power levels, whereas 3p-DABSRC suffers from more severe reactive power loss at high power levels. Therefore, employing 3p-DABSRC for low to medium power levels and 3p-DABRIC for high power levels can help to improve the overall power conversion efficiency for a wide range of output voltage and power levels.

B. Comparison of Output Line Currents $I_{2\mathrm{A,rms}}$

The expressions for the rms output line currents $I_{2\mathrm{A,rms}}$ for both configurations are as follows:

$$I_{2\mathrm{A,rms(3p-DABRIC)}} = \sqrt{\frac{1}{2\pi}\int_0^{2\pi}[i_{2\mathrm{A(3p-DABRIC)}}(t)]^2 d\omega t}$$

$$= \frac{2\sqrt{6}\, V_{\mathrm{in}} Y_{\mathrm{3p-DABRIC}} \cos(\alpha)}{n\pi} \quad (26)$$

$$I_{2\mathrm{A,rms(3p-DABSRC)}} = \sqrt{\frac{1}{2\pi}\int_0^{2\pi}[i_{2\mathrm{A(3p-DABSRC)}}(t)]^2 d\omega t}$$

$$= \frac{(\sqrt{2V_{\mathrm{o}}^2 n^2 - 8V_{\mathrm{in}}V_{\mathrm{o}} n\cos(\beta) + 8V_{\mathrm{in}}^2})Y_{\mathrm{3p-DABSRC}}}{n\pi}. \quad (27)$$

Fig. 7(d)–(f) plots the output line currents $I_{2\mathrm{A,rms(3p-DABRIC)}}$ and $I_{2\mathrm{A,rms(3p-DABSRC)}}$ versus normalized output power $P_{\mathrm{o,p.u.}}$ for $G = 0.5$, 1.0, and 1.5, respectively using expressions (8), (12), (26), and (27). It is clear from Fig. 7(d)–(f) that $I_{2\mathrm{A,rms(3p-DABRIC)}}$ is always smaller than $I_{2\mathrm{A,rms(3p-DABSRC)}}$ for all the three cases due to UPF operation of 3p-DABRIC. Moreover, as the output phase voltages of 3p-DABRIC are not modulated, the secondary bridge of 3p-DABRIC does not suffer from circulating current or reactive power loss which explains the reason for lower $I_{2\mathrm{A,rms(3p-DABRIC)}}$ compared to $I_{2\mathrm{A,rms(3p-DABSRC)}}$. The difference between the output line currents for the two configurations becomes more distinctive at higher power levels when the external phase-shift angle β of 3p-DABSRC increases accompanied by an increase in reactive power loss. Moreover, as $I_{2\mathrm{A,rms(3p-DABRIC)}}$ is independent of V_{o}, $I_{2\mathrm{A,rms(3p-DABRIC)}}$ remains the same for all three cases. For 3p-DABSRC, $I_{2\mathrm{A,rms(3p-DABSRC)}}$ is the same as $I_{1\mathrm{A,rms(3p-DABSRC)}}$ for all the three cases [cf. Fig. 7(a)–(c)] since $I_{1\mathrm{A,rms(3p-DABSRC)}} = I_{2\mathrm{A,rms(3p-DABSRC)}}$ in a series resonant network.

Upon comparison of the line currents for both configurations under varying output power and voltage levels [cf. Fig. 7(a)–(f)], it is clear that $I_{2\mathrm{A,rms(3p-DABRIC)}}$ is always smaller than $I_{2\mathrm{A,rms(3p-DABSRC)}}$. However, the input line current $I_{1\mathrm{A,rms}}$ for both configurations intersect with each other at a particular output power level that is a function of V_{o}. The intersection point where the input line currents for both configurations cross each other can serve as a parameter to determine the preferred network configuration. By comparing the input line currents $I_{1\mathrm{A,rms}}$ for the entire output power range for a particular value of V_{o}, determining the intersection point and then repeating the same procedure for the entire output voltage range, boundary can be drawn to obtain the regions where the input line current for one configuration is smaller than the input line current for the other configuration, as shown in Fig. 8(a). It can be seen from Fig. 8(a) that for any particular value of G, $I_{1\mathrm{A,rms(3p-DABSRC)}}$ is greater than $I_{1\mathrm{A,rms(3p-DABRIC)}}$ for higher power levels, whereas for operation below $G \leq 0.5$, $I_{1\mathrm{A,rms(3p-DABRIC)}}$ is always smaller than $I_{1\mathrm{A,rms(3p-DABSRC)}}$.

C. Comparison of Soft-Switching Range

As it has been well established in the literature that for 3p-DAB converter, the switches in the primary bridge will undergo soft commutation when the input line current $i_{1\mathrm{A}}(t)$ lags the primary bridge phase voltage $v_{1\mathrm{A}}(t)$, and the switches in the secondary bridge will experience soft commutation when the output line current $i_{2\mathrm{A}}(t)$ leads the secondary bridge phase voltage $v_{2\mathrm{A}}(t)$ [23]. It has been demonstrated in [20], [24] that 3p-DABRIC can achieve full-range ZVS operation irrespective of voltage conversion ratio when both internal and external phase-shift angles are used to modulate output power according to $\alpha = \beta$. However, when external phase-shift angle β is kept 0° and internal phase-shift angle α is used to modulate output power and achieve UPF operation, the switches in the lagging leg of each phase in the primary bridge will undergo hard commutation.

For the case of 3p-DABSRC, it can perform full-range ZVS operation only for unity voltage conversion ratio in which case the desired condition $\theta = \frac{\beta}{2}$ always holds. However, for non-unity voltage conversion ratio, the ZVS range of 3p-DABSRC becomes restricted, and depending on the degree of variation in voltage conversion ratio, its ZVS region can shrink significantly as shown in Fig. 8(b).

D. Power Loss Model

To gain a better insight about the performance and power loss breakdown for both configurations over wide output voltage and output power range, the power loss model developed in [25] was adapted to calculate the power losses for both configurations over the entire output voltage range. In this way, the boundary for switching between two configurations can be identified on the basis of minimum power loss. The said power loss model includes conduction loss P_{Cond} in passive elements and switches, switching loss P_{Sw} arising from hard switching and core loss P_{Core} in magnetics as illustrated in the following:

$$P_{\mathrm{L}} = P_{\mathrm{Cond}} + P_{\mathrm{Sw}} + P_{\mathrm{Core}}. \quad (28)$$

The power loss breakdown for both configurations for G= 0.5, 1.0, and 1.5 are shown in Fig. 9(a)–(f). It is clear from Fig. 9(a)–(f). that, for both configurations, conduction loss has the dominant contribution in the overall power loss under all output voltage and output power levels. As 3p-DABRIC has lower output line current $I_{2\mathrm{A,rms}}$ for the entire output voltage range as

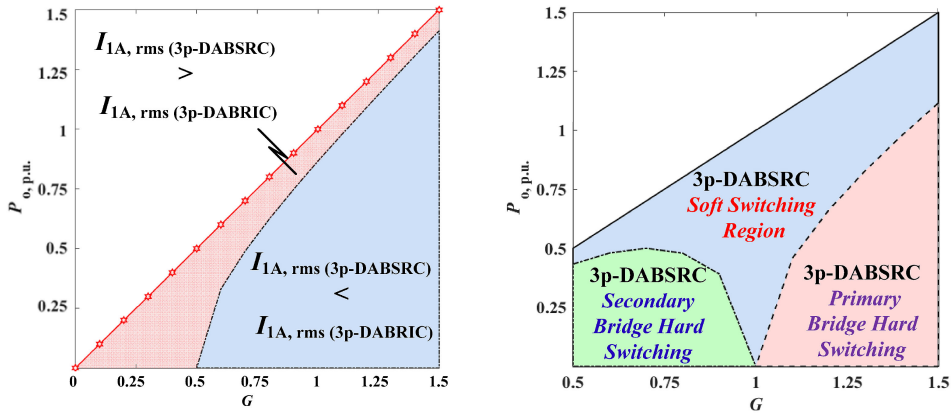

(a) (b)

Fig. 8. (a) Regions highlighting lower input line current $I_{1A,rms}$ values among the 3p-DABRIC and 3p-DABSRC for the entire output voltage and power range. (b) Regions showing hard-switching and soft-switching range for 3p-DABSRC for entire output voltage and power range.

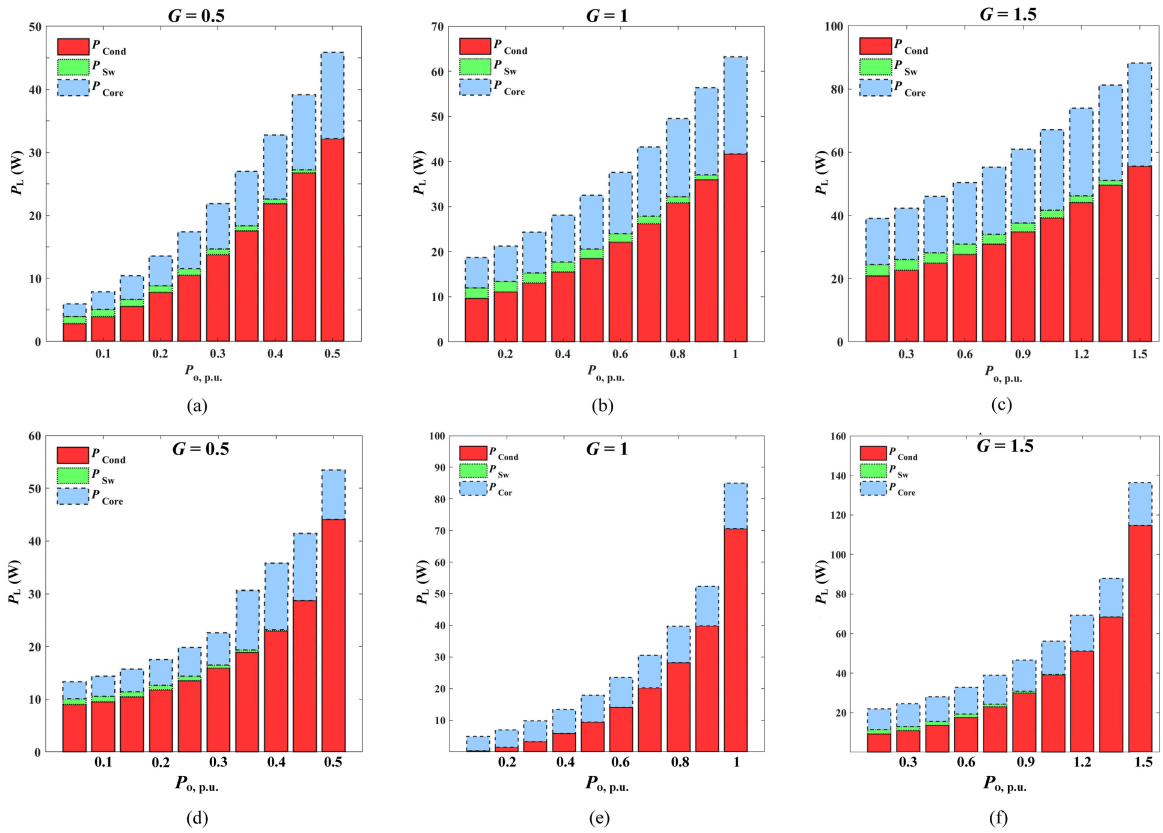

Fig. 9. Power loss breakdown for 3p-DABRIC considering (a) $G = 0.5$; (b) $G = 1$; (c) $G = 1.5$; power loss breakdown for 3p-DABSRC considering (d) $G = 0.5$; (e) $G = 1$; (f) $G = 1.5$.

compared to 3p-DABSRC, the contribution of output line current $I_{2A,rms}$ to the total conduction loss will have a larger impact on 3p-DABSRC as compared to 3p-DABRIC. However, the input line currents $I_{1A,rms}$ for both configurations intersect with each other and its impact on the conduction loss in both configurations depends on both voltage conversion ratio and output power level. Fig. 10(a)–(c) illustrates a comparison between the conduction loss of both configurations versus normalized output power $P_{o,p.u.}$ for $G = 0.5$, 1.0, and 1.5. From Fig. 10(a), it is clear that for $G = 0.5$, the conduction loss in 3p-DABSRC is higher as compared to 3p-DABRIC for the entire output power range, attributed mainly to the higher $I_{1A,rms(3p-DABSRC)}$. From Fig. 10(b)–(c), it can be seen that for $G > 0.5$, the conduction loss in 3p-DABRIC dominates at lower power levels while it becomes dominant at higher power levels in 3p-DABSRC. For a particular value of V_o, (28) can be applied to calculate the total power loss for both configurations over the entire output power range and the intersection point

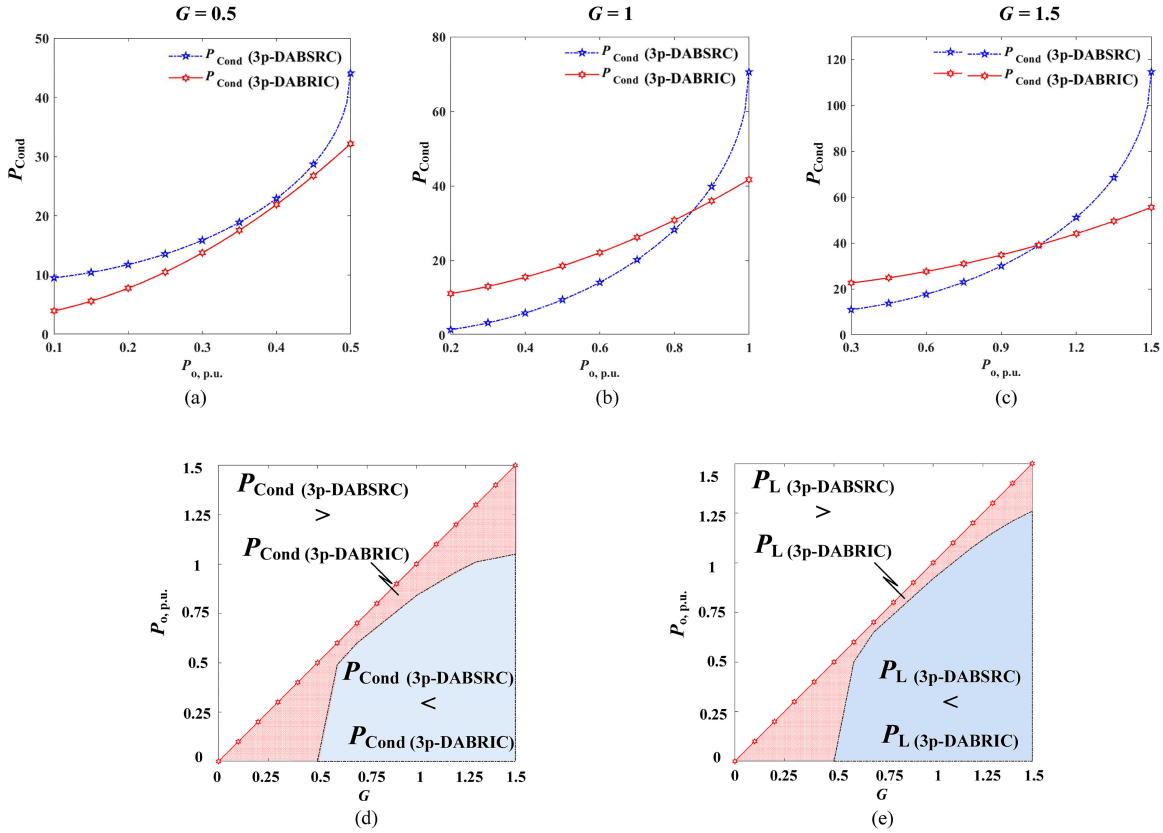

Fig. 10. Comparison of conduction loss $P_{\rm Cond}$ between the 3p-DABRIC and 3p-DABSRC for (a) $G = 0.5$; (b) $G = 1$; (c) $G = 1.5$. (d) Regions highlighting lower conduction loss $P_{\rm Cond}$ among the 3p-DABRIC and 3p-DABSRC for the entire output voltage and power range. (e) Regions highlighting lower total power loss $P_{\rm L}$ among the 3p-DABRIC and 3p-DABSRC for the entire output voltage and power range.

where the two power loss curves intersect with each other can be subsequently determined. By repeating the same procedure for the entire output voltage range, the boundary defining the region with a lower power loss can be obtained. Fig. 10(d)–(e) demonstrates the region characterized by a lower conduction loss and lower total power loss below the calculated boundary. The regions plotted in Fig. 10(d)–(e) are in compliance with the findings obtained from comparison of input and output line currents for both configurations, i.e., (for high power levels and $G \leq 0.5$, 3p-DABRIC outperforms 3p-DABSRC, whereas for low to medium power levels and $G > 0.5$, 3p-DABSRC leads to a lower power loss). Furthermore, by comparing Fig. 10(d)–(e) with Fig. 8(a), it can be observed that the boundaries defining the regions of lower input line currents $I_{\rm 1A,rms}$, lower conduction loss $P_{\rm Cond}$, and lower total power loss $P_{\rm L}$ exhibit similar trends. Therefore, it can be safely concluded that input line currents $I_{\rm 1A,rms}$ play a distinctive role in the efficiency performance of both configurations. Hence, the proposed converter should primarily operate as 3p-DABSRC at low to medium output power levels and switch to 3p-DABRIC to achieve a higher efficiency at higher power levels.

E. Experimental Results

To verify the theoretical analysis presented above, experimental results are collected from a laboratory prototype, as shown in Fig. 11, built with the specifications given in Table I. Fig. 12(a)–(f) depicts the experimental waveforms of a 3p-DABSRC for three different output power levels (i.e., 100%, 80%, and 60% of the rated power) for $G = 1$. For 3p-DABSRC, external phase-shift angle β is used as the control variable to modulate output power while internal phase-shift angle α is kept at 0°. It can be observed from Fig. 12(a)–(f) that as β is increased to achieve a higher output power level, the phase displacement between line current and phase voltage increases leading to a higher line current and hence a higher conduction loss. Moreover, it can be

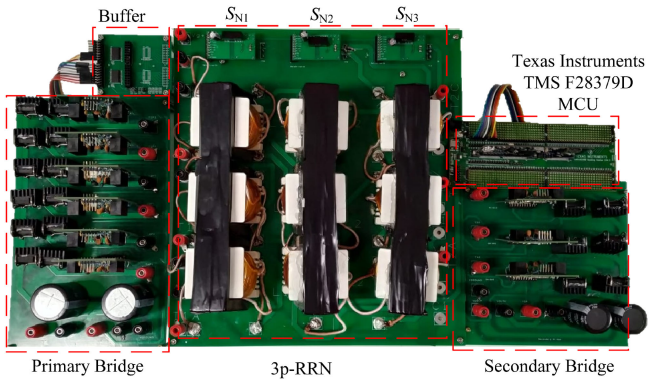

Fig. 11. Laboratory prototype of proposed resonant-type 3p-DAB converter.

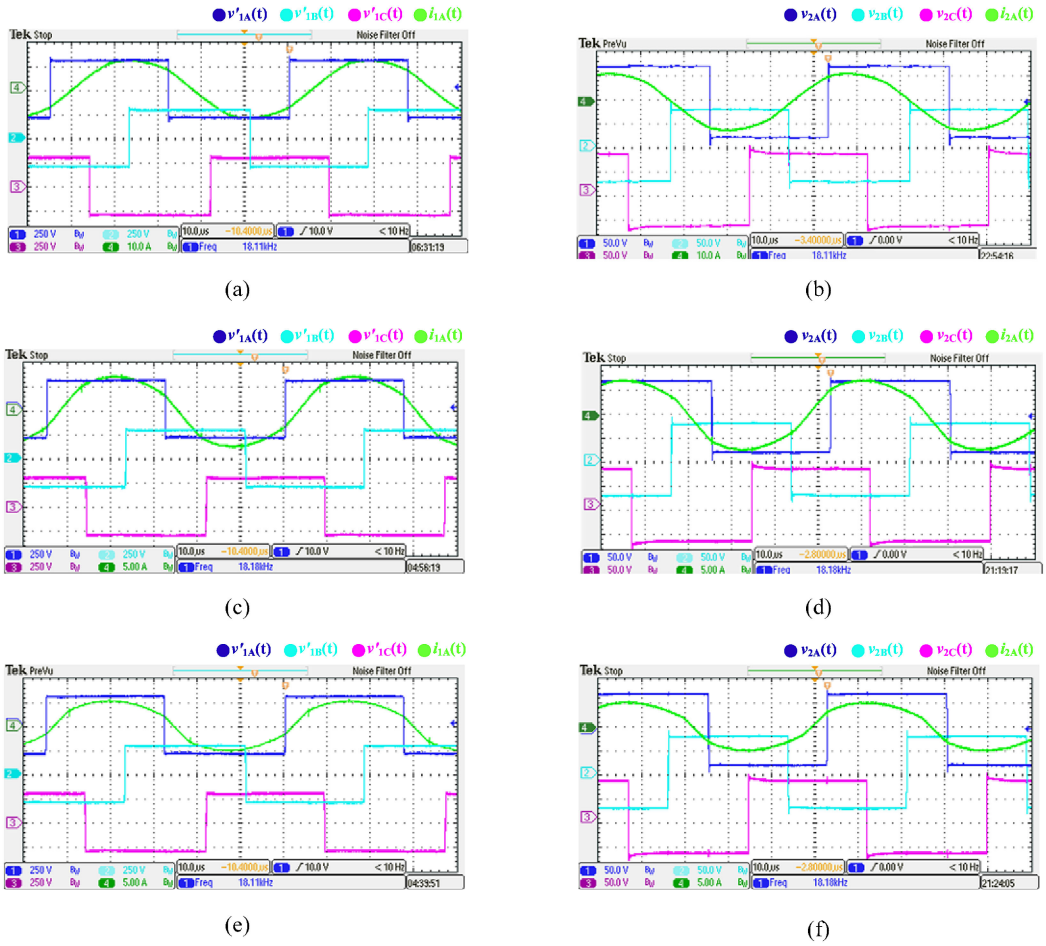

Fig. 12. Experimental waveforms for 3p-DABSRC considering $V_{\rm in} = 300$ V, $V_{\rm o} = 150$ V, and $G = 1$: (a) input phase voltages $v'_{\rm 1A}(\rm t)$, $v'_{\rm 1B}(\rm t)$, and $v'_{\rm 1C}(\rm t)$ on the primary side of the transformer and the input line current $i_{\rm 1A}(\rm t)$ at rated power having $I_{\rm o} = 10$ A and $\beta = 90°$; (b) output phase voltages $v_{\rm 2A}(\rm t)$, $v_{\rm 2B}(\rm t)$, and $v_{\rm 2C}(\rm t)$ with respect to dc bus midpoint and the output line current $i_{\rm 2A}(\rm t)$ at rated power having $I_{\rm o} = 10$ A and $\beta = 90°$; (c) input phase voltages $v'_{\rm 1A}(\rm t)$, $v'_{\rm 1B}(\rm t)$, and $v'_{\rm 1C}(\rm t)$ on the primary side of the transformer at 80%-rated power having $I_{\rm o} = 8$ A and $\beta = 53.13°$; (d) output phase voltages $v_{\rm 2A}(\rm t)$, $v_{\rm 2B}(\rm t)$, and $v_{\rm 2C}(\rm t)$ with respect to dc bus midpoint at 80%-rated power having $I_{\rm o} = 8$ A and $\beta = 53.13°$; (e) input phase voltages $v'_{\rm 1A}(\rm t)$, $v'_{\rm 1B}(\rm t)$, and $v'_{\rm 1C}(\rm t)$ on the primary side of the transformer and the input line current $i_{\rm 1A}(\rm t)$ at 60%-rated power having $I_{\rm o} = 6$ A and $\beta = 36.8°$; and (f) output phase voltages $v_{\rm 2A}(\rm t)$, $v_{\rm 2B}(\rm t)$, and $v_{\rm 2C}(\rm t)$ with respect to dc bus midpoint at 60%-rated power having $I_{\rm o} = 6$ A and $\beta = 36.8°$.

seen that all switches in the primary and secondary bridges are soft switched for $G = 1$.

Fig. 13(a)–(f) depicts the experimental waveforms of 3p-DABRIC for the same three output power levels as Fig. 12(a)–(f). For this configuration, internal phase-shift angle α is used as the control variable while the external phase-shift angle β is kept at 0°. Modulation of α effectively modulates the duty cycle of the input phase voltages which in turn modulates output power. It can be observed from Fig. 13(a)–(f) that 3p-DABRIC maintains UPF at the input and output ports of 3p-RIN. However, due to the existence of zero voltage level in the input phase voltages, the primary bridge of 3p-DABRIC suffers from non-zero circulating current, whereas since the secondary bridge voltages are not modulated, there is no zero voltage level in the output phase voltages and hence no circulating current and reactive power loss in the secondary bridge. Moreover, as discussed earlier, the switches in the lagging leg of each phase in the primary bridge are hard switched. Recall that this configuration can achieve full-range ZVS operation for all switches when modulated with $\beta = \alpha$ [20]. However, doing so will result in a substantial increase in line currents and conduction loss. Therefore, full-range ZVS operation of 3p-DABRIC is not considered here. Fig. 14(a)–(b) depicts the experimental waveforms of 3p-DABSRC while Fig. 14(c)–(d) shows the experimental waveforms of 3p-DABRIC for $G = 0.5$ and 30% rated power. It can be seen from Fig. 14(b) that for 3p-DABSRC at lower power levels and G=0.5, the output line current $i_{\rm 2A}(t)$ lags the output phase voltage $v_{\rm 2A}(t)$ leading to hard switching in the secondary-side switches.

The power conversion efficiencies for 3p-DABRIC and 3p-DABSRC are plotted in Fig. 15(a)–(f) for $G = 0.25$, 0.5, 0.75, 1.0, 1.25, and 1.5, respectively. It is evident from Fig. 15(a)–(f) that the measured power conversion efficiency curves are consistent with those predicted by applying the power loss model, thus verifying the accuracy of the power loss model. The minor mismatches between the measured and calculated efficiencies are attributed to some unmodeled losses, such as PCB trace resistances, capacitor equivalent series resistance (ESR), connecting

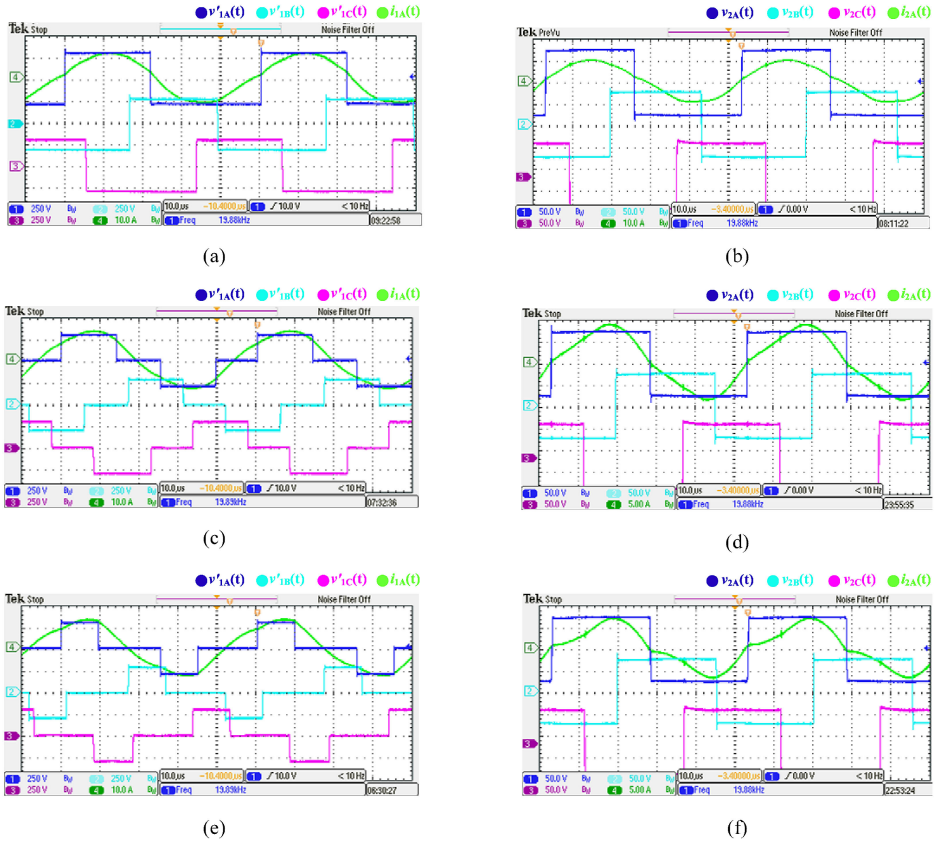

Fig. 13. Experimental waveforms for 3p-DABRIC considering $V_{\rm in} = 300$ V, $V_{\rm o} = 150$ V, and $G = 1$: (a) input phase voltages $v'_{1\rm A}(\rm t)$, $v'_{1\rm B}(\rm t)$, and $v'_{1\rm C}(\rm t)$ on the primary side of the transformer and the input line current $i_{1\rm A}(\rm t)$ at rated power having $I_{\rm o} = 10$ A and $\alpha = 0°$; (b) output phase voltages $v_{2\rm A}(\rm t)$, $v_{2\rm B}(\rm t)$, and $v_{2\rm C}(\rm t)$ with respect to dc bus midpoint and the output line current $i_{2\rm A}(\rm t)$ at rated power having $I_{\rm o} = 10$ A and $\alpha = 0°$; (c) input phase voltages $v'_{1\rm A}(\rm t)$, $v'_{1\rm B}(\rm t)$, and $v'_{1\rm C}(\rm t)$ on the primary side of the transformer at 80%-rated power having $I_{\rm o} = 8$ A and $\alpha = 36.87°$; (d) output phase voltages $v_{2\rm A}(\rm t)$, $v_{2\rm B}(\rm t)$, and $v_{2\rm C}(\rm t)$ with respect to dc bus midpoint at 80%-rated power having $I_{\rm o} = 8$ A and $\alpha = 36.87°$; (e) input phase voltages $v'_{1\rm A}(\rm t)$, $v'_{1\rm B}(\rm t)$, $v'_{1\rm C}(\rm t)$ on the primary side of the transformer and the input line current $i_{1\rm A}(\rm t)$ at 60%-rated power having $I_{\rm o} = 6$ A and $\alpha = 53.13°$; (f) output phase voltages $v_{2\rm A}(\rm t)$, $v_{2\rm B}(\rm t)$, and $v_{2\rm C}(\rm t)$ with respect to dc bus midpoint at 60%-rated power having $I_{\rm o} = 6$ A and $\alpha = 53.13°$.

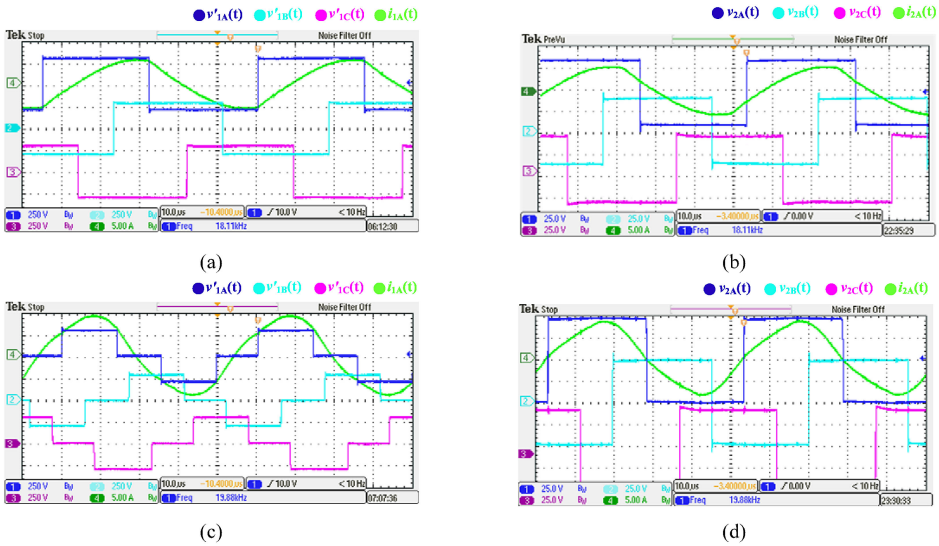

Fig. 14. Experimental waveforms for 3p-DABSRC considering $V_{\rm in} = 300$ V, $V_{\rm o,min} = 75$ V, and $G_{\rm min} = 0.5$: (a) input phase voltages $v'_{1\rm A}(\rm t)$, $v'_{1\rm B}(\rm t)$, and $v'_{1\rm C}(\rm t)$ on the primary side of the transformer and the input line current $i_{1\rm A}(\rm t)$ at 30%-rated power having $I_{\rm o} = 4$ A and $\beta = 23.48°$; (b) output phase voltages $v_{2\rm A}(\rm t)$, $v_{2\rm B}(\rm t)$, and $v_{2\rm C}(\rm t)$ with respect to dc bus midpoint and the output line current $i_{2\rm A}(\rm t)$ at 30%-rated power having $I_{\rm o} = 4$ A and $\beta = 23.48°$; (c) Experimental waveforms for 3p-DABRIC configuration considering $V_{\rm in} = 300$ V, $V_{\rm o,min} = 75$ V and $G_{\rm min} = 0.5$ showing input phase voltages $v'_{1\rm A}(\rm t)$, $v'_{1\rm B}(\rm t)$, and $v'_{1\rm C}(\rm t)$ on the primary side of the transformer at 30%-rated power having $I_{\rm o} = 4$ A and $\alpha = 66.4°$; (d) output phase voltages $v_{2\rm A}(\rm t)$, $v_{2\rm B}(\rm t)$, and $v_{2\rm C}(\rm t)$ with respect to dc bus midpoint at 30%-rated power having $I_{\rm o} = 4$ A and $\alpha = 66.4°$.

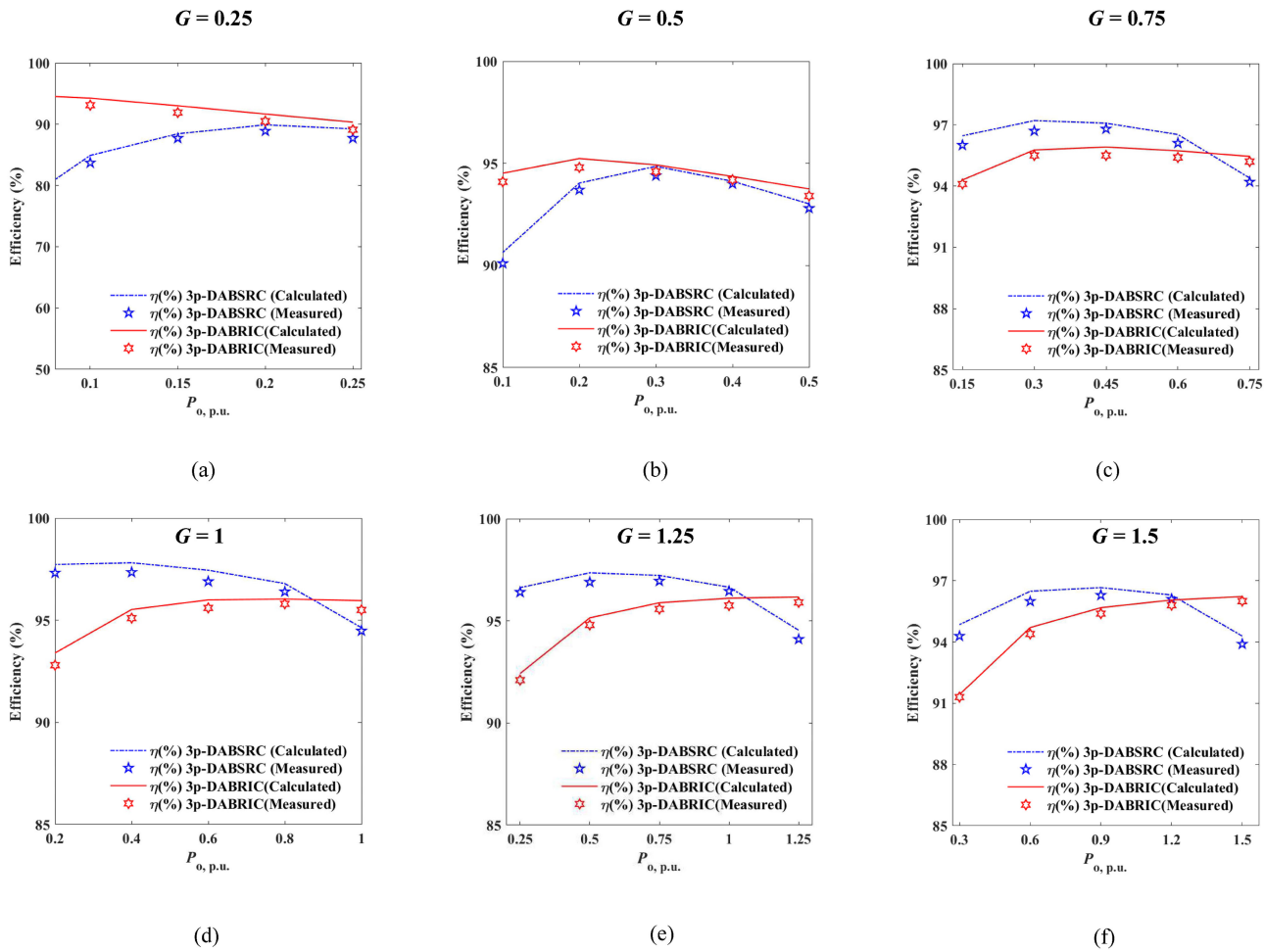

Fig. 15. Comparison of power conversion efficiency η between the 3p-DABRIC and 3p-DABSRC for (a) $G = 0.25$; (b) $G = 0.5$; (c) $G = 0.75$ (d) $G = 1$; (e) $G = 1.25$; (f) $G = 1.5$.

wires resistance, etc. From the efficiency curves, it can be seen that 3p-DABRIC exhibits a higher power conversion efficiency as compared to 3p-DABSRC at all power levels for $G < 0.5$ [cf. Fig. 15(a)–(b)] and at higher power levels only for $G > 0.5$ [cf. Fig. 15(c)–(f)], whereas 3p-DABSRC always performs better in terms of power conversion efficiency at low to medium power levels as compared to 3p-DABRIC for $G > 0.5$ [cf. Fig. 15(c)–(f)]. The combination of both operation modes, therefore, leads to a wide range high-efficiency performance under wide range variations in output voltage and power levels.

F. Performance Analysis for Higher Switching Frequencies

3p-DABRIC can offer full range ZVS operation irrespective of wide range variations in the output voltage and power levels but at the expense of increased circulating current leading to more severe conduction loss. Unless the operating frequency is sufficiently high, the benefits gained from the soft-switching operation of 3p-DABRIC are neutralized by the increase in conduction loss associated with higher line currents under full ZVS operation mode. To allow a more detailed comparison between the three operation modes (i.e., 3p-DABSRC, 3p-DABRIC-UPF, and 3p-DABRIC-ZVS) at increased switching frequencies, loss modeling is done for ZVS operation mode of 3p-DABRIC. The switching frequencies selected for the analysis are 50 and 150 kHz, and for each switching frequency two voltage conversion ratios, i.e. ,$G = 0.5$ and 1.0 are considered. The results obtained for 50 kHz are shown below in Fig. 16. It can be seen from Fig. 16(a)–(b) that the ZVS operation mode has relatively higher line current leading to higher conduction loss as shown in Fig. 16(c)–(d). Moreover, it can also be seen from Fig. 16(c)–(d) that the conduction loss associated with ZVS operation is the most dominant power loss among the three operation modes at 50 kHz. The total power loss for the three operation modes at 50 kHz is shown in Fig. 16(e)–(f) where it can be seen that ZVS operation mode incurs a higher total power loss as compared to the other operation modes over a wide range of output power.

Similar analysis for 150 kHz operation is shown in Fig. 17. As the line currents remain unchanged at higher switching frequencies, the line currents for 150 kHz operation are not plotted in Fig. 17. For operation at 150 kHz, switching loss dominates for most of the output power range for both cases of $G = 0.5$ and 1.0 and ZVS operation leads to a lower total

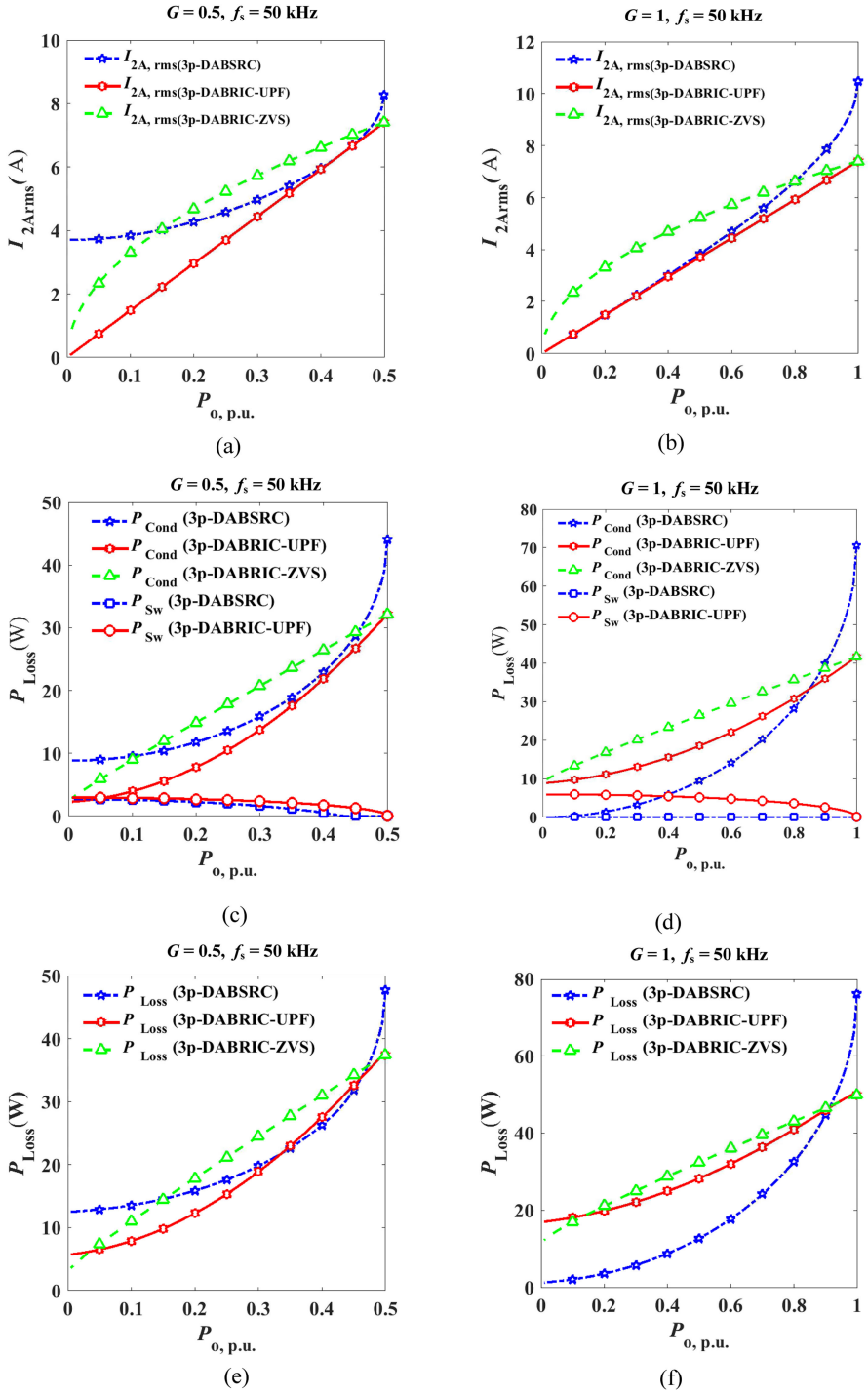

Fig. 16. (a) Line current comparison between the three modes of operation for $G = 0.5$, $f_s = 50$ kHz; (b) Line current comparison between the three modes of operation for $G = 1.0$, $f_s = 50$ kHz. (c) Power loss distribution (conduction loss and switching loss) between the three modes of operation for $G = 0.5$, $f_s = 50$ kHz. (d) Power loss distribution (conduction loss and switching loss) between the three modes of operation for $G = 1.0$, $f_s = 50$ kHz. (e) Power loss comparison between the three modes of operation for $G = 0.5$, $f_s = 50$ kHz. (f) Power loss comparison between the three modes of operation for $G = 1.0$, $f_s = 50$ kHz.

power loss as compared to UPF operation [cf. Fig. 17(d)]. It can, therefore, be safely concluded that conduction loss is the dominant loss mechanism for operation at moderate switching frequencies and UPF operation gives rise to a lower total power loss as compared to ZVS operation. However, for operation at higher switching frequencies, switching loss becomes dominant over conduction loss and ZVS operation gives rise to a lower total power loss than UPF operation. Depending on the particular operating frequency and power/current rating selected, the operation mode of the proposed converter can be flexibly reconfigured to minimize the total power loss for achieving wide range high-efficiency performance.

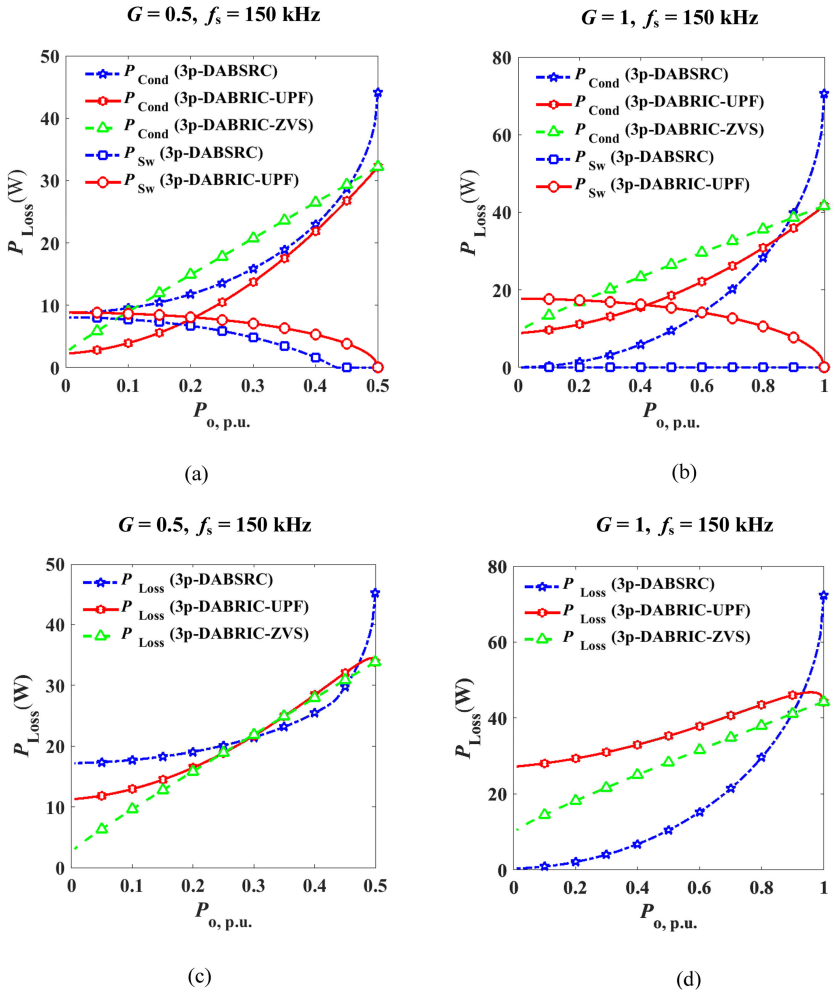

Fig. 17. (a) Power loss distribution (conduction loss and switching loss) between the three modes of operation for $G = 0.5$, $f_s = 150$ kHz. (b) Power loss distribution (conduction loss and switching loss) between the three modes of operation for $G = 1.0$, $f_s = 150$ kHz. (c) Power loss comparison between the three modes of operation for $G = 0.5$, $f_s = 150$ kHz. (d) Power loss comparison between the three modes of operation for $G = 1.0$, $f_s = 150$ kHz.

VI. Conclusion

This article has proposed a structurally reconfigurable resonant-type three-phase dual-active-bridge (3p-DAB) dc–dc converter. The proposed converter utilizes a 3p-RRN that operates either as a 3p-DABRIC or as a 3p-DABSRC under different output voltage and output power levels. The ability to transform between two resonant networks offers greater freedom in the shaping of the efficiency performance of 3p-DAB converter. For the selected specifications, it has been found that 3p-DABRIC outperforms 3p-DABSRC in terms of efficiency at higher power levels, whereas 3p-DABSRC performs better at lower power levels. It is also found that the dominant loss mechanism in 3p-DAB converter is the conduction loss arising from circulating current (for 3p-DABRIC) or reactive power flow (for 3p-DABSRC). The idea of reconfigurable 3p-DAB converter as a means to achieve wide range high-efficiency performance is both theoretically and experimentally verified.

References

[1] G. Waltrich, M. A. M. Hendrix, and J. L. Duarte, "Three-phase bidirectional dc/dc converter with six inverter legs in parallel for EV applications," *IEEE Trans. Ind. Electron.*, vol. 63, no. 3, pp. 1372–1384, Mar. 2016.

[2] L. Xue, D. Diaz, Z. Shen, F. Luo, P. Mattavelli, and D. Boroyevich, "Dual active bridge based battery charger for plug-in hybrid electric vehicle with charging current containing low frequency ripple," *IEEE Trans. Power Electron.*, vol. 30, no. 12, pp. 7299–7307, Dec. 2015.

[3] B. Zhao, Q. Song, L. Jianguo, and W. Liu, "A modular-multilevel-DC-link front-to-front DC transformer based on high-frequency dual active phase-shift for HVDC grid integration," *IEEE Trans. Ind. Electron.*, vol. 64, no. 11, pp. 8919–8927, Nov. 2017.

[4] H. Shi *et al.*, "Minimum-backflow-power scheme of DAB-based solid-state transformer with extended-phase-shift control," *IEEE Trans. Ind. Appl.*, vol. 54, no. 4, pp. 3483–3496, Jul./Aug. 2018.

[5] F. Xue, R. Yu, and A. Q. Huang, "A 98.3 % efficient GaN isolated bidirectional storage system applications," *IEEE Trans. Ind. Electron.*, vol. 64, no. 11, pp. 9094–9103, Nov. 2017.

[6] Y. Lu, Q. Wu, Q. Wang, D. Liu, and L. Xiao, "Analysis of a novel zero-voltage-switching bidirectional dc–dc converter for energy storage system," *IEEE Trans. Power Electron.*, vol. 33, no. 4, pp. 3169–3179, Apr. 2018. [Online]. Available: http://ieeexplore.ieee.org/document/7927459/

[7] Q. Ye, R. Mo, and H. Li, "Low-frequency resonance suppression of a dual-active-bridge dc–dc converter enabled dc microgrid," *IEEE J. Emerg. Sel. Topics Power Electron.*, vol. 5, no. 3, pp. 982–994, Sep. 2017.

[8] B. Zhao, Q. Song, and W. Liu, "A practical solution of high-frequency-link bidirectional solid-state transformer based on advanced components in hybrid microgrid," *IEEE Trans. Ind. Electron.*, vol. 62, no. 7, pp. 4587–4597, Jul. 2015.

[9] M. C. Kisacikoglu, M. Kesler, and L. M. Tolbert, "Single-phase on-board bidirectional PEV charger for V2G reactive power operation," *IEEE Trans. Smart Grid*, vol. 6, no. 2, pp. 767–775, Mar. 2015.

[10] U. K. Madawala and D. J. Thrimawithana, "A bidirectional inductive power interface for electric vehicles in V2G systems," *IEEE Trans. Ind. Electron.*, vol. 58, no. 10, pp. 4789–4796, Oct. 2011.
[11] R. W. De Doncker, D. M. Divan, and M. H. K. Kheraluwala, "A three-phase soft-switched high-power-density dc–dc converter for high-power applications," *IEEE Trans. Ind. Appl.*, vol. 27, no. 1, pp. 63–73, Jan./Feb. 1991.
[12] Z. Biao, Y. Qingguang, and S. Weixin, "Extended-phase-shift control of isolated bidirectional dc– dc converter for power distribution in microgrid," *IEEE Trans. Power Electron.*, vol. 27, no. 11, pp. 4667–4680, Nov. 2012.
[13] H. M. De Oliveira Filho, D. D. S. Oliveira, and P. P. Praça, "Steady-state analysis of a ZVS bidirectional isolated three-phase dc–dc converter using dual phase-shift control with variable duty cycle," *IEEE Trans. Power Electron.*, vol. 31, no. 3, pp. 1863–1872, Mar. 2016.
[14] J. Hu, N. Soltau, and R. W. D. Doncker, "Asymmetrical duty-cycle control of three-phase dual-active bridge converter for soft-switching range extension," in *Proc. Energy Convers. Congr. Expo.*, 2016, pp. 1–8.
[15] M. Yaqoob, K. H. Loo, and Y. M. Lai, "Extension of soft-switching region of dual-active-bridge converter by a tunable resonant tank," *IEEE Trans. Power Electron.*, vol. 32, no. 12, pp. 9093–9104, Dec. 2017. [Online]. Available: http://ieeexplore.ieee.org/document/7820224/
[16] J. Kan, S. Xie, Y. Tang, and Y. Wu, "Voltage-fed dual active bridge bidirectional dc– dc converter with an immittance network," *IEEE Trans. Power Electron.*, vol. 29, no. 7, pp. 3582–3590, Jul. 2014.
[17] R. P. Twiname, D. J. Thrimawithana, U. K. Madawala, and C. A. Baguley, "A dual-active bridge topology with a tuned CLC network," *IEEE Trans. Power Electron.*, vol. 30, no. 12, pp. 6543–6550, Dec. 2015.
[18] T. Jiang, J. Zhang, X. Wu, K. Sheng, and Y. Wang, "A bidirectional LLC resonant converter with automatic forward and backward mode transition," *IEEE Trans. Power Electron.*, vol. 30, no. 2, pp. 757–770, Feb. 2015.
[19] J. H. Jung, H. S. Kim, M. H. Ryu, and J. W. Baek, "Design methodology of bidirectional CLLC resonant converter for high-frequency isolation of DC distribution systems," *IEEE Trans. Power Electron.*, vol. 28, no. 4, pp. 1741–1755, Apr. 2013.
[20] A. Z. Khan, K. H. Loo, and Y. M. Lai, "Design, analysis, and performance characterization of dual-active-bridge dc–dc converter utilizing three-phase resonant immittance network," *IEEE Trans. Power Electron.*, vol. 34, no. 2, pp. 1159–1180, Feb. 2018.
[21] H. Irie and T. Nishisako, "Three-phase immittance converter," *Elect. Eng. Jpn.*, vol. 145, no. 1, pp. 52–58, 2003. [Online]. Available: http://doi.wiley.com/10.1002/eej.10169
[22] R. Mirzahosseini and F. Tahami, "A phase-shift three-phase bidirectional series resonant dc–dc converter," in *Proc. IEEE 37th Annu. Conf. Ind. Electron. Soc.*, 2011, pp. 1137–1143.
[23] H. Van Hoek, "Design and operation considerations of three-phase dual active bridge converters for low-power applications with wide voltage ranges," Ph.D. dissertation, Faculty Elect. Eng. Inf. Technol., RWTH Aachen Univ., Aachen, Germany, 2016.
[24] A. Z. Khan and K. H. Loo, "A three-phase dual-active-bridge dc–dc immittance converter," in *Proc. IEEE Energy Convers. Congr. Expo.*, 2018, pp. 6336–6343.
[25] F. Krismer and J. Kolar, "Accurate power loss model derivation of a high-current dual active bridge converter for an automotive application," *IEEE Trans. Ind. Electron.*, vol. 57, no. 3, pp. 881–891, Mar. 2010.

Akif Zia Khan (S'15) received the B.Eng. degree in electrical engineering from the National University of Sciences and Technology (NUST), Islamabad, Pakistan, in 2011, and the M.Sc. degree in electric power systems from the North China Electric Power University, Beijing, China, in 2014. He is currently working toward the Ph.D. degree in the area of power electronics at The Hong Kong Polytechnic University, Hong Kong.

He has been a Visiting Ph.D. Scholar with the Center of Reliable Power Electronics, Department of Energy Technology, Aalborg University, Aalborg, Denmark. From 2014 to 2016, he has served as a Lecturer with the U.S.-Pakistan Center for Advanced Studies in Energy, NUST, Islamabad, Pakistan. During the Spring of 2016, he was a Visiting Research Scholar with the Power Systems Engineering Research Center, Arizona State University, Tempe, AZ, USA. His current research interests include design, modeling, and control of high-power and high-frequency bidirectional resonant power converters for various power-processing applications.

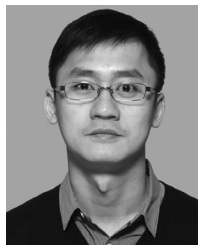

K. H. Loo (S'97–M'99) received the B.Eng. (Hons.) in electronic engineering and the Ph.D. degree from the University of Sheffield, Sheffield, U.K., in 1999 and 2002, respectively.

Upon completion of his doctoral degree, he won the Japan Society for the Promotion of Science (JSPS) Postdoctoral Fellowship and worked as Postdoctoral Researcher with Ehime University, Matsuyama, Japan, from 2002 to 2004. He joined The Hong Kong Polytechnic University in 2006 where he is now an Associate Professor with the Department of Electronic and Information Engineering. His research interests include high-frequency power conversion, in particular power converters for renewable energy systems.

Dr. Loo has been an Associate Editor for the IEEE TRANSACTIONS ON ENERGY CONVERSION since 2013 and the IEEE POWER ENGINEERING LETTERS since 2015, and contributes regularly as Reviewer for various international journals and conferences. He is currently the Chair of the Power Electronics and Control Sub-Committee of the IEEE Technical Committee on Transportation Electrification.